CHALMERS
UNIVERSITY OF TECHNOLOGY

Modal analysis of vortex rope using dynamic mode decomposition

Citation for the original published paper (version of record):
Salehi, S., Nilsson, H. (2024). Modal analysis of vortex rope using dynamic mode decomposition. Physics of Fluids, 36(2). http://dx.doi.org/10.1063/5.0186871

RESEARCH ARTICLE | FEBRUARY 23 2024

Modal analysis of vortex rope using dynamic mode decomposition

Saeed Salehi ; Håkan Nilsson

Physics of Fluids 36, 024122 (2024)
https://doi.org/10.1063/5.0186871

Physics of Fluids ARTICLE pubs.aip.org/aip/pof

Modal analysis of vortex rope using dynamic mode decomposition

Cite as: Phys. Fluids **36**, 024122 (2024); doi: 10.1063/5.0186871
Submitted: 9 November 2023 · Accepted: 24 January 2024 ·
Published Online: 23 February 2024

Saeed Salehi[1,2,a] and **Håkan Nilsson**[1]

AFFILIATIONS

[1]Division of Fluid Dynamics, Department of Mechanics and Maritime Sciences, Chalmers University of Technology, Gothenburg SE-412 96, Sweden
[2]Chalmers Industriteknik, Gothenburg, Sweden

[a]Author to whom correspondence should be addressed: saeed.salehi@chalmers.se

ABSTRACT

The decelerating swirling flow in the draft tube of hydraulic turbines at part load conditions often results in a self-induced instability known as vortex rope. This phenomenon is associated with detrimental pressure pulsations in the hydropower system that need to be mitigated. A deep understanding of such instability is essential for developing effective mitigation and control strategies. The current article exploits the dynamic mode decomposition (DMD) algorithm to perform an in-depth modal analysis of the physical aspects of the vortex rope. DMD can efficiently identify distinct coherent structures with isolated frequencies. The sparsity-promoting variant of DMD is exploited to extract the most influential modes. The computational fluid dynamics (CFD) data is generated via a resolved improved delayed detached eddy simulation using OpenFOAM. Frequency analysis of the CFD data uncovered peaks at the normalized frequencies of $f/f_n = 0.56$ and 0.63, whose origins seemed initially unclear. Nevertheless, the DMD modal analysis elucidates that these excitations are associated with the rotation of the reunited vortex and fluctuations of the separated boundary layer, respectively. The non-linear dynamics of the flow field are unveiled through a modal decomposition revealing distinctive coherent structures with isolated frequencies. These include rotational and plunging modes of the vortex rope, traveling wakes of the blades, boundary layer separation due to strong adverse pressure gradient, and a reunited vortex core. The flow field reconstruction through time dynamics of DMD modes highlights while it is possible to achieve a perfect flow field reconstruction considering all recovered modes, the model typically fails to predict future behavior with an acceptable level of accuracy. The chaotic nature of the resolved turbulent flow field presents a substantial challenge for predicting the future through a model built based on prior events. The current modal analysis not only provides a more comprehensive understanding of the physics underlying the vortex rope phenomenon but also lays the groundwork for potential future applications in controlling mechanisms.

I. INTRODUCTION

The utilization of renewable electrical energy sources has witnessed rapid growth due to their availability and environment friendliness to meet the consistently growing global energy demand. However, energy resources such as solar and wind are intermittent, as their output depends on sunlight and wind availability and can vary significantly in a short period of time. Such intermittency necessitates the integration of controllable energy sources into the electrical grid.[1] In the contemporary energy landscape, this goal is achieved through the integration of hydropower systems which can store energy for later use and play a crucial role in providing the necessary flexibility to balance the electrical grid over various time scales.[2,3]

Hydraulic turbines, originally designed for operating at the steady best efficiency point (BEP), are now operated in various off-design conditions and during transient sequences to stabilize the electrical grid. Steady off-design conditions can be grouped up as part load (PL), high load (HL), full load (FL), and runaway conditions. In theory, hydraulic turbines are designed so that the runner extracts all the angular momentum generated by the guide vanes at the BEP condition. Thus, operating at off-design conditions leaves a large residual angular momentum at the runner exit, which can be positive (same direction as the runner rotation) or negative (opposite direction). The residual swirl enters the conical part of the draft tube where the flow decelerates. Decelerating swirling flow in the draft tube often results in vortex breakdown and hydrodynamic instabilities that may lead to unsteady phenomena such as a processing helical vortex structure, also known as the PL vortex rope,[4] or a torch-like axisymmetric vortex structure at HL condition.[5] The instability of the residual swirl can particularly be significant in turbines with a fixed runner blade pitch angle (such as Francis or propeller turbines), while it can be partially reduced by the adjustable runner blade angles in Kaplan turbines.

The vortex rope phenomenon is a self-induced instability that is associated with severe pressure pulsations in the hydropower system. Such pulsations could be especially damaging if the frequency of the vortex rope matches one of the natural frequencies of the system. In the case of Francis turbines operating at PL condition, the main frequency of the vortex rope pulsations has been mostly identified in the range of 0.2–0.4 times the runner rotation frequency, sometimes known as Rheingan's frequency of the system.[6] The vortex rope instability and its effects on the vibrations of the turbines have been extensively studied in the literature and shown to cause detrimental structural vibrations.[7–11] Such vibrations can develop fatigue damage and seriously affect the lifetime of the turbine, which leads to tremendous economic losses.[12] Consequently, designing flow control strategies to mitigate the emergence of such hydrodynamic instabilities becomes immensely valuable for enhancing the operational versatility of hydro turbines in a sustainable manner.

The implementation of an axial flow jet injection from the runner crown has demonstrated notable effectiveness in mitigating the formation of vortex ropes.[13] However, a thorough comprehension of the draft tube instabilities is a fundamental requirement for devising effective and optimum flow control strategies. Numerous attempts have been reported in the literature to understand and describe the underlying physics of the part load draft tube instability. It is assumed that the vortex rope instability is closely connected to the vortex breakdown phenomenon, which is usually known as a significant sudden change in the structure of the vortex core.[14–20] Different researchers have employed analytical,[21–23] numerical,[24–29] and experimental[30–35] methods to understand and describe the vortex rope instability in the draft tube of Francis turbines.

A linear global stability analysis of the time-averaged flow field has been utilized to characterize the vortex rope as a global unstable eigenmode.[36] Similar to spiral vortex breakdown, a single-helix disturbance was shown to emerge around the time-averaged flow field and evolve over time to eventually form the vortex rope.

The significant growth of computational power has led to a wide utilization of data-driven and machine-learning algorithms in fluid dynamics. Consequently, the model order reduction methods are used to extract the fundamental features of flow fields. Such feature discovery algorithms can play a crucial role in understanding complex flow regimes such as the vortex rope instability and to describe them through their underlying coherent structures. The main intention of such algorithms is to reduce the dimensionality of a complex system without significant information loss and represent it as a low-dimensional approximation through the identification of the principal patterns.

The most popular method for extracting spatial patterns in fluid dynamics applications is proper orthogonal decomposition (POD),[37–40] which is also known as principal component analysis or Karhunen–Loève decomposition in other principles. POD operates on snapshots of a mean-subtracted flow field (i.e., fluctuating field) and represents the data through a number of extracted features, i.e., POD modes, that are spatially orthogonal. The modes vary in time through their corresponding time coefficients. A few researchers have employed POD to investigate the vortex rope instability.[41–44] Štefan *et al.*[42] used POD to assess the effectiveness of injecting axial flow for active flow control of the vortex rope. POD was able to represent a low-dimensional approximation of the system through a limited number of modes and also to clarify the effect of axial injection on the eigenmodes.

The dynamic mode decomposition (DMD)[45,46] method is another widely used technique, closely connected to the Koopman analysis,[47] that analyzes time snapshots of the flow field and extracts the flow patterns. The extracted modes, unlike POD, are not spatially orthogonal and oscillate harmonically with specific frequencies. In other words, POD provides structures that are spatially orthogonal while DMD focuses on temporal orthogonality.[46] Despite their similarities, POD and DMD are fundamentally different as POD modes are associated with many different frequencies while each DMD mode oscillates with an isolated frequency. In that sense, the DMD modes are more realistic physical representations of flow patterns, i.e., coherent structures. DMD can particularly be utilized for the identification of flow patterns, low-order representation of flow field, or prediction of the future based on the current data set.

There has been a significant effort in the literature to improve the accuracy and robustness of both POD and DMD algorithms, which is not the concern of the current study to thoroughly review. However, we employ a variant of DMD known as sparsity-promoting DMD (SPDMD)[48] that takes advantage of compressed sensing concepts to extract a subset of the most influential subset of DMD modes.

Since its introduction, the DMD algorithm has been applied to a variety of engineering flow applications, such as turbomachinery,[49–51] aerodynamics,[52–54] heat transfer,[55,56] and marine.[57–59] However, to the best of the authors' knowledge, the DMD method has not been adopted for modal analysis and flow pattern extraction of self-induced instability of decelerated swirling flows in draft tubes of hydraulic turbines. Therefore, the current study performs a modal decomposition of the vortex rope instability through DMD. First, the flow field is studied in detail through a resolved improved delayed detached eddy simulation (IDDES) simulation and the fundamental physics of the flow field is explained. Then, the DMD analysis is performed, and the DMD modes and eigenvalues are extracted. The DMD results are connected to physical observations of the flow field. Additionally, a POD analysis is also carried out on the data set to compare with the DMD results.

The rest of the paper is organized as follows. Section II describes the theory of the employed modal decomposition algorithms, i.e., DMD and SPDMD. The configuration of the studied flow field and the numerical aspects of the computational fluid dynamics (CFD) simulations are presented in Secs. III and IV, respectively. Section V verifies and describes the CFD and modal analysis results. The paper is finally summarized and conclusions are drawn in Sec. VI.

II. THEORY OF DYNAMIC MODE DECOMPOSITION

The DMD algorithm[46] starts by collecting a sequence of data snapshots from CFD or experimental measurements. Assume that $\boldsymbol{x}_i$ is a single-column matrix consisting of flow field data, such as velocity, pressure, and temperature, in different locations at time i. In the case of using multiple flow field quantities, they can be stacked vertically to form one column. In general, the vector $\boldsymbol{x}_i$ contains M complex components, i.e., $\boldsymbol{x}_i \in \mathbb{C}^M$, in which M is the number of measurement points in space. Recording the data at different equispaced times with time step Δt, a full matrix of the flow field data at all times and space locations is constructed as

$$\boldsymbol{X} = [\boldsymbol{x}_0, \boldsymbol{x}_1, \ldots, \boldsymbol{x}_{N-1}, \boldsymbol{x}_N] \in \mathbb{C}^{M\times(N+1)}. \tag{1}$$

Each column of matrix $\boldsymbol{X}$ represents a snapshot of the flow field data at a specific time, whereas each row stores the time variation of the flow field for one single location in space. The full sequence of data could form two matrices as

$$\begin{aligned} \boldsymbol{X}_0 &= [\boldsymbol{x}_0, \boldsymbol{x}_1, \ldots, \boldsymbol{x}_{N-2}, \boldsymbol{x}_{N-1}] \in \mathbb{C}^{M\times N}, \\ \boldsymbol{X}_1 &= [\boldsymbol{x}_1, \boldsymbol{x}_2, \ldots, \boldsymbol{x}_{N-1}, \boldsymbol{x}_N] \in \mathbb{C}^{M\times N}. \end{aligned} \tag{2}$$

For fluid flows, typically the number of point locations is much larger than the number of time snapshots ($M \gg N$), and thus, $\boldsymbol{X}_1$ and $\boldsymbol{X}_0$ are tall rectangular matrices.

Assuming that the dynamical system that maps time i to $i+1$ is linear and time-invariant, there exists a matrix $\boldsymbol{A}$ that enables

$$\boldsymbol{x}_{i+1} = \boldsymbol{A}\boldsymbol{x}_i. \tag{3}$$

Substituting Eq. (3) into Eq. (2) yields

$$\boldsymbol{X}_1 = \boldsymbol{A}\boldsymbol{X}_0. \tag{4}$$

In the case of a non-linear dynamical system, the above assumption can be considered as a linear approximation. Since M is usually large, the matrix $\boldsymbol{A} \in \mathbb{C}^{M\times M}$ contains a substantial number of complex components. Therefore, the main goal of DMD analysis is to discover a low-order approximation of the matrix $\boldsymbol{A}$ that can represent the dynamics of the data with sufficient accuracy.

If the matrix of snapshots $\boldsymbol{X}_0$ is of rank r, an optimal low-rank representation of the matrix $\boldsymbol{A}$, namely, $\tilde{\boldsymbol{A}} \in \mathbb{C}^{r\times r}$, spanned by the POD modes of $\boldsymbol{X}_0$, can be constructed as

$$\boldsymbol{A} \approx \boldsymbol{U}\tilde{\boldsymbol{A}}\boldsymbol{U}^*, \tag{5}$$

where $\boldsymbol{U}$ is the POD modes of $\boldsymbol{X}_0$ and $\boldsymbol{U}^*$ is its conjugate transpose. $\boldsymbol{U}$ can be obtained through an economy singular value decomposition (SVD) of $\boldsymbol{X}_0$,[48] i.e.,

$$\boldsymbol{X}_0 = \boldsymbol{U}\boldsymbol{\Sigma}\boldsymbol{V}^*, \tag{6}$$

where $\boldsymbol{\Sigma}$ is an $r \times r$ diagonal matrix containing r non-zero singular values $[\sigma_1, \sigma_2, \ldots, \sigma_r]$, and $\boldsymbol{U} \in \mathbb{C}^{M\times r}$ and $\boldsymbol{V} \in \mathbb{C}^{r\times N}$ are orthonormal matrices, meaning $\boldsymbol{U}\boldsymbol{U}^* = I$ and $\boldsymbol{V}\boldsymbol{V}^* = I$. The low-order approximation of the mapping matrix $\boldsymbol{A}$ can be calculated by combining Eqs. (4)–(6), yielding

$$\tilde{\boldsymbol{A}} = \boldsymbol{U}^*\boldsymbol{X}_1\boldsymbol{V}\boldsymbol{\Sigma}^{-1}. \tag{7}$$

Using the matrix of POD modes $\boldsymbol{U}$, the high-dimensional data $\boldsymbol{x}_i$ can be mapped into a lower-dimensional space as $\boldsymbol{z}_i = \boldsymbol{U}^*\boldsymbol{x}_i$. Thus, inserting $\boldsymbol{x}_i = \boldsymbol{U}\boldsymbol{z}_i$ and Eq. (5) into Eq. (3) gives

$$\boldsymbol{z}_{i+1} = \tilde{\boldsymbol{A}}\boldsymbol{z}_i. \tag{8}$$

Therefore, the full rank matrix $\boldsymbol{A}$ maps the high-dimensional data $\boldsymbol{x}_i$ to the next time snapshot while the low-order representation $\tilde{\boldsymbol{A}}$ maps the reduced order system $\boldsymbol{z}_i$. Eigendecomposition of $\tilde{\boldsymbol{A}}$ reads

$$\tilde{\boldsymbol{A}} = \boldsymbol{W}\boldsymbol{\Lambda}\boldsymbol{W}^{-1}, \tag{9}$$

where $\boldsymbol{W}$ is a matrix whose columns are eigenvectors of $\tilde{\boldsymbol{A}}$, i.e., $\boldsymbol{w}_j$, and $\boldsymbol{\Lambda}$ is a diagonal matrix whose non-zero elements are the eigenvalues of $\tilde{\boldsymbol{A}}$, i.e., λ_j. Therefore, the ith snapshot of the low-order system $\boldsymbol{x}_i$ is calculated as

$$\boldsymbol{z}_i = \boldsymbol{W}\boldsymbol{\Lambda}^i\boldsymbol{W}^{-1}\boldsymbol{z}_0 \tag{10}$$

and hence, the ith snapshot of the high-dimensional data can be reconstructed through

$$\boldsymbol{x}_i = \boldsymbol{U}\boldsymbol{W}\boldsymbol{\Lambda}^i\boldsymbol{W}^{-1}\boldsymbol{U}^*\boldsymbol{x}_0. \tag{11}$$

One can approximate the data by the linear combination of DMD modes $\boldsymbol{\phi}_j = \boldsymbol{U}\boldsymbol{w}_j$, and $\boldsymbol{\Phi} = \boldsymbol{U}\boldsymbol{W}$ can be defined as a matrix containing all the DMD modes. In Eq. (11), $\boldsymbol{W}^{-1}\boldsymbol{U}^*\boldsymbol{x}_0$ is an $r \times 1$ vector, usually called the mode amplitude vector $\boldsymbol{\alpha} = [\alpha_1, \alpha_2, \ldots, \alpha_r]^{\mathrm{T}}$, whose jth element denotes the modal contribution of the corresponding DMD mode to the initial condition (first snapshot $\boldsymbol{x}_0$). Consequently,

$$\boldsymbol{x}_i = \boldsymbol{\Phi}\boldsymbol{\Lambda}^i\boldsymbol{\alpha} \tag{12}$$

and then the matrix $\boldsymbol{X}_0$ can be reconstructed as

$$\boldsymbol{X}_0 = \boldsymbol{\Phi}\boldsymbol{D}_{\boldsymbol{\alpha}}\boldsymbol{V}_{\mathrm{and}}, \tag{13}$$

where $\boldsymbol{D}_{\boldsymbol{\alpha}} = \mathrm{diag}(\boldsymbol{\alpha})$ and $\boldsymbol{V}_{\mathrm{and}} \in \mathbb{C}^{r\times N}$ is the Vandermonde matrix defined as

$$\boldsymbol{V}_{\mathrm{and}} = \begin{bmatrix} 1 & \lambda_1 & \lambda_1^2 & \ldots & \lambda_1^{N-1} \\ 1 & \lambda_2 & \lambda_2^2 & \ldots & \lambda_2^{N-1} \\ \vdots & \vdots & & \ddots & \vdots \\ 1 & \lambda_r & \lambda_r^2 & \ldots & \lambda_r^{N-1} \end{bmatrix}. \tag{14}$$

A. Finding amplitudes of the DMD modes

One can find the unknown mode amplitude vector $\boldsymbol{\alpha}$ through a least squares fit or regression of all the sampled data. Alternatively, the optimal mode amplitude can be obtained by solving an optimization problem built upon Eq. (13) as

$$\boldsymbol{\alpha}_{\mathrm{opt}} = \arg\min_{\boldsymbol{\alpha}} ||\boldsymbol{X}_0 - \boldsymbol{\Phi}\boldsymbol{D}_{\boldsymbol{\alpha}}\boldsymbol{V}_{\mathrm{and}}||_{\mathrm{F}}^2, \tag{15}$$

where $||\cdot||_{\mathrm{F}}$ is the Frobenius norm. Employing $\boldsymbol{X}_0 = \boldsymbol{U}\boldsymbol{\Sigma}\boldsymbol{V}^*$ and $\boldsymbol{\Phi} = \boldsymbol{U}\boldsymbol{W}$, the optimization problem can be rewritten as

$$\boldsymbol{\alpha}_{\mathrm{opt}} = \arg\min_{\boldsymbol{\alpha}} \; J(\boldsymbol{\alpha}), \tag{16}$$

where

$$J(\boldsymbol{\alpha}) = ||\boldsymbol{\Sigma}\boldsymbol{V}^* - \boldsymbol{W}\boldsymbol{D}_{\boldsymbol{\alpha}}\boldsymbol{V}_{\mathrm{and}}||_{\mathrm{F}}^2. \tag{17}$$

Jovanović, Schmid, and Nichols[48] presented the analytical solution to optimal amplitudes of DMD modes as

$$\boldsymbol{\alpha}_{\mathrm{opt}} = \left((\boldsymbol{W}^*\boldsymbol{W})\bigcirc\left(\overline{\boldsymbol{V}_{\mathrm{and}}\boldsymbol{V}_{\mathrm{and}}^*}\right)\right)^{-1}\overline{\mathrm{diag}(\boldsymbol{V}_{\mathrm{and}}\boldsymbol{V}\boldsymbol{\Sigma}^*\boldsymbol{W})} \tag{18}$$

in which $\bigcirc$ denotes the elementwise multiplication of matrices. Acquiring an optimal solution to the mode amplitude completes the DMD procedure and not only valuable information about coherent structures of the flow is discovered, but the future flow field that is not solved (or measured) can also be predicted.

The accuracy of the recovered solution can be assessed by comparing the reconstructed field and the original data. Accordingly, the performance loss is defined as follows:

$$\Pi_{\text{loss}} = 100\sqrt{\frac{J(\boldsymbol{\alpha})}{J(\mathbf{0})}} = 100\frac{||\boldsymbol{X}_0 - \boldsymbol{\Phi}\boldsymbol{D}_{\boldsymbol{\alpha}}\boldsymbol{V}_{\text{and}}||_{\text{F}}}{||\boldsymbol{X}_0||_{\text{F}}}. \tag{19}$$

B. Sparsity-promoting DMD

It is usually desirable to find and extract a subset of DMD modes that has the most influential role in the dynamics of the system rather than considering the full set of modes. Sparsity-promoting[48] DMD (SPDMD) is proposed to seek a sparse solution to the optimization problem of Eq. (16). The method works in two steps, namely, (1) seeking a sparse structure with a trade-off between the number of modes and the approximation error and subsequently, (2) fixing the sparsity of the structure and finding the corresponding optimal amplitudes of the modes. Figure 1 displays this trade-off, i.e., how the increasing sparsity of the DMD solution can affect the accuracy of the reconstructed signal.

In order to push the solution of Eq. (16) toward sparser answers, the cardinality of $\boldsymbol{\alpha}$ can be utilized as an additional term to the equation to penalize the number of non-zero elements, as

$$\boldsymbol{\alpha}_{\text{opt}} = \arg\min_{\boldsymbol{\alpha}} \left(J(\boldsymbol{\alpha}) + \gamma||\boldsymbol{\alpha}||_0\right), \tag{20}$$

where $||\boldsymbol{\alpha}||_0$ is the ℓ_0 norm of $\boldsymbol{\alpha}$, i.e., the cardinality, and γ is the regularization parameter that determines the level of the sparsity of the solution as a higher value of γ enhances the sparsity of solution. The optimization problem in Eq. (20) has a non-convex objective function and is NP-hard to compute.[60] Such optimization problems are usually translated into a computationally tractable problem by replacing $||\cdot||_0$ with its convex relaxation $||\cdot||_1$ and solving

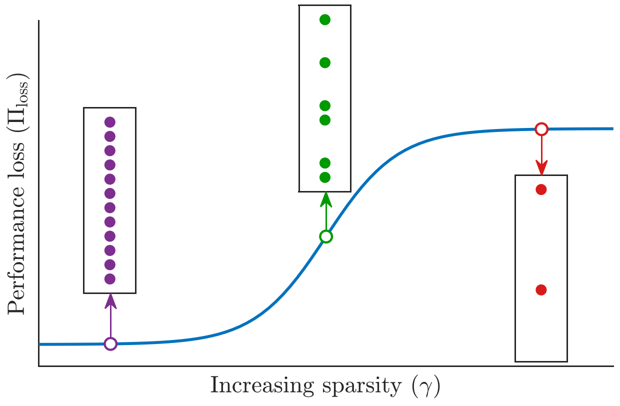

FIG. 1. Effect of the sparsity of the DMD solution on the performance loss. The rectangles are symbolic representations of the recovered solution matrix, with non-zero members shown as dots.

$$\boldsymbol{\alpha}_{\text{opt}} = \arg\min_{\boldsymbol{\alpha}} \left(J(\boldsymbol{\alpha}) + \gamma||\boldsymbol{\alpha}||_1\right). \tag{21}$$

The above is a convex optimization problem that could be solved using standard optimization methods. In this study, the efficient algorithm developed by Jovanović, Schmid, and Nichols[48] that utilizes the alternating direction method of multipliers (ADMM)[61] is adopted to solve the optimization problem. The details of the algorithm are not presented here and readers are referred to Ref. 48 for more information.

C. Frequency analysis

For the sake of analysis, a new variable can be defined as $\mu_j = \ln(\lambda_j)/\Delta t$ where λ_j is the jth eigenvalue of $\tilde{\boldsymbol{A}}$. Accordingly, Eq. (12) can be reformulated as

$$\boldsymbol{x}_i = \boldsymbol{\Phi}\exp(\boldsymbol{\Omega}t)\boldsymbol{\alpha}, \tag{22}$$

where $\boldsymbol{\Omega} = \text{diag}(\boldsymbol{\mu})$, and t is the physical time at ith time step, i.e., $t = i\Delta t$. The current change of variable helps us to provide a frequency interpretation of the DMD results. Note that μ is a complex variable with real and imaginary parts, i.e., $\mu = \sigma + i\omega$. Equation (22) indicates that for a pseudo-periodic dynamical system, the real part of μ_j (σ_j) corresponds to the growth or decay rate of jth mode, while its imaginary part (ω_j) correlates with the frequency of the mode. Thereby, the underlying frequency of the jth mode reads

$$f_j = \frac{\text{imag}(\mu_j)}{2\pi} = \frac{\omega_j}{2\pi}. \tag{23}$$

D. Mode sorting algorithm

The DMD modes that are calculated through the classical full DMD algorithm are not necessarily sorted and one needs to order them to select the dominant modes. The simplest way of sorting the DMD modes is to order them based on the amplitude of the first snapshot, i.e., $\boldsymbol{\alpha}$. Although the approach is straightforward to implement, it can fail to find the dominant coherent structure, especially in the case of transient unstable flows.

An improved criterion for mode sorting is to consider the complete time evolution of the amplitude of each mode.[62] The amplitude of mode j at time step i is $b_{ij} = \lambda_j^i\alpha_j$. Thus, the time integration of the amplitude of mode j is

$$I_j = \int |b_j(t)|\ \mathrm{d}t = \int |b_{ij}|\ \mathrm{d}t. \tag{24}$$

Here, I_j denotes the impact of the jth mode on the whole sampling space, and the modes are sorted based on its magnitude.

III. FLOW CONFIGURATION

The present work considers the Timisoara swirl generator (TSG) as the investigated case. The apparatus was developed to study the self-induced instabilities of decelerated swirling flows that can occur in part load conditions of hydraulic turbines.[13,63]

Figure 2 presents a three-dimensional view of the TSG model that consists of four main parts, i.e., leaned struts, guide vanes, runner, and convergent–divergent pipe. Water flows between the leaned struts to reach 13 fixed guide vanes that direct the flow toward the runner with a proper angle of attack. The axial-flow runner has ten blades. The primary purpose of the runner is to redistribute the total pressure

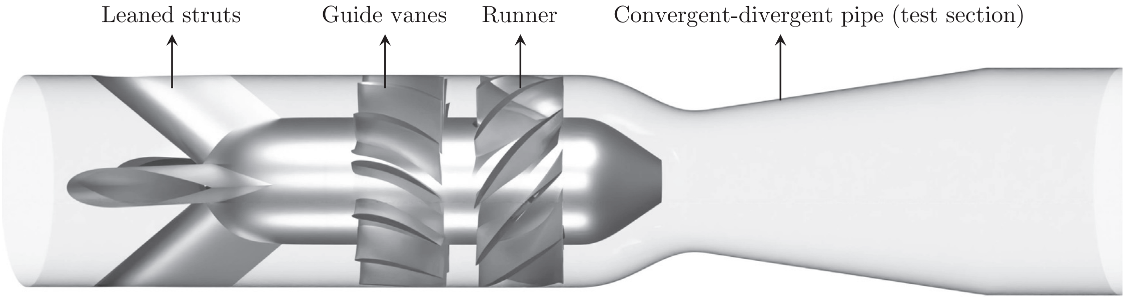

FIG. 2. Full computational domain of the Timisoara swirl generator.

by generating an excess in axial velocity near the shroud while simultaneously creating a corresponding deficit near the hub.[13] This behavior resembles that of a Francis turbine operating under PL conditions. There exists a small gap, approximately 0.4 mm wide, between the blade tip and the shroud. However, the velocity profiles experimentally measured downstream the runner did not indicate any significant effects of the leakage flow. This observation was further supported by numerical results derived both with and without the runner blade tip clearances.[64] Accordingly, the runner blade tip clearances are not considered in the current study.

The convergent–divergent pipe downstream the runner includes a conical test section with a cone angle of $2 \times 8.6^\circ = 17.2^\circ$. It resembles the discharge cone of Francis turbines and is the main region of interest in the experimental measurements. A two-dimensional cross section view of the test section is displayed in Fig. 3. W_0, W_1, and W_2 are the lines where velocity profiles are experimentally measured, while MG0, MG1, MG2, and MG3 represent the level at which the pressure sensors are placed.

In the experimental test rig, the rotational speed of the runner may be reduced through a magnetorheological brake.[65] The current study considers the runaway condition in which the runner rotates freely with no torque. At this condition, the flow rate is set to $Q = 30$ l/s which corresponds to the runaway rotational speed of 920 rpm. More details on the TSG test case and the available measured data are found through `openfoamwiki.net/index.php/Sig_Turbomachinery_/_Timisoara_Swirl_Generator`.

IV. PHYSICAL AND NUMERICAL ASPECTS OF THE CFD FRAMEWORK

This section describes both physical (e.g., turbulence modeling) and numerical (e.g., CFD code, discretization, pressure velocity coupling, parallel processing, etc.) aspects of the CFD framework of the current study.

The governing equations are discretized using the finite volume method on a collocated mesh employing the OpenFOAM-v2112 open-source CFD software.[66,67] Sections IV A–IV G present a detailed description of the numerical aspects of the adopted CFD framework. It is worth mentioning that the current CFD model is developed based on the open-source model,[68] provided by the OpenFOAM turbomachinery working group.

A. Turbulence modeling

A hybrid Reynolds-averaged Navier–Stokes (RANS)-large eddy simulation (LES) approach is employed for turbulence modeling through the improved delayed detached eddy simulation (IDDES)[69] technique that utilizes the low-Reynolds Spalart–Allmaras RANS model for the closure. Historically the detached eddy simulation (DES) model was first developed as a hybrid RANS-LES model to take advantage of the accuracy of large eddy simulations and low computational costs of RANS modes.[70] It was originally intended for flows with a thin boundary layer solved through RANS with elongated grid cells followed by a massively separated flow field modeled with LES on ideally

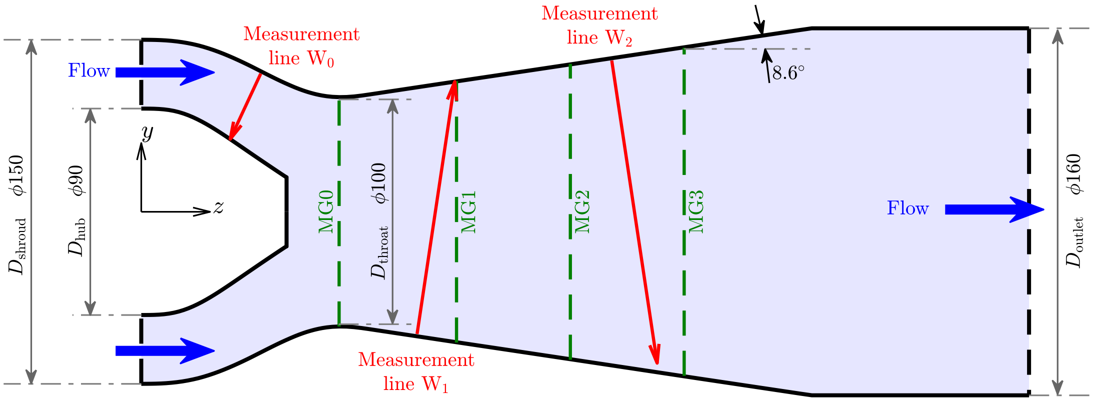

FIG. 3. Cross section of the test section of the TSG model, showing PIV measurement lines W_0, W_1, and W_2 and pressure sensor locations MG0, MG1, MG2, and MG3. All dimensions are in mm.

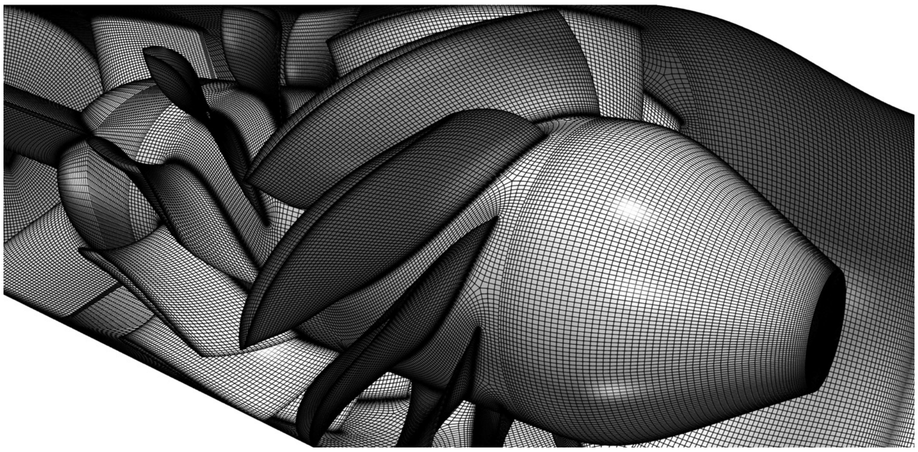

FIG. 4. Overview of the computational mesh. Here, the coarsest mesh (Level 1 with 9.3×10^6 cells) is only displayed for better illustration. The finer meshes utilize the same block topology.

isotropic cells. However, the model failed to accurately predict turbulent flows with thick boundary layers and shallow separation regions. Therefore, the delayed DES (DDES) model was developed[71] to address this issue and reduce the immense sensitivity of DES to the grid spacing parallel to the walls. However, both the DES and DDES methods suffer from the log-layers mismatch problem that can cause an underprediction of the skin friction by up to 15%–20%.[69] To overcome this problem, the improved DDES (IDDES) model was proposed[69,72–74] by combining DDES and wall-modeled LES (WMLES) capabilities.

The definition of the sub-grid scale in the IDDES model reads

$$\Delta = \min[\max(C_\mathrm{w} d_\mathrm{w}, C_\mathrm{w} h_\mathrm{max}, h_\mathrm{wn}), h_\mathrm{max}], \tag{25}$$

where d_w is the distance from the nearest wall, $h_\mathrm{max} = \max(h_x, h_y, h_z)$ is the maximum local grid spacing, h_wn is the grid spacing in the wall-normal direction, and C_w is an empirical constant whose value is set to 0.15.

The length scale in the turbulent viscosity ($\tilde{\nu}$) transport equation of the IDDES model is defined as

$$l_\mathrm{IDDES} = \tilde{f}_d (1 + f_e) l_\mathrm{RANS} + (1 - \tilde{f}_d) l_\mathrm{LES} \tag{26}$$

in which $\tilde{f}_d$ and f_e are the blending and elevating functions introduced by Shur *et al.*[69] l_RANS is the RANS length scale that is the wall distance (d_w) in the Spalart–Allmaras model. The LES length scale, l_LES, is also defined via sub-grid scale Δ as

$$l_\mathrm{LES} = C_\mathrm{DES} \Psi \Delta, \tag{27}$$

where C_DES is the fundamental empirical constant of the DES model,[75] and Ψ is a low-Reynolds correction term.[71]

The selection of the present IDDES model stems from a comprehensive set of experimental simulations aimed at thoroughly examining the impact of various turbulence models, such as unsteady RANS (URANS), DES, and LES models, in this particular test case. The IDDES model was ultimately chosen for the modal analysis due to its balanced accuracy and computational cost. These findings are not included in the article to ensure the main focus remains on the article's primary objective, namely, the physical and modal analysis of the flow field.

B. Computational mesh

The full computational domain of the TSG model is divided into four regions, namely, the struts, guide vanes, runner, and convergent–divergent pipe (test section). A block-structured mesh is generated for each region separately, and the meshes are merged together within OpenFOAM. The struts and test section regions are meshed in ICEM-CFD, while the guide vanes and the runner meshes are produced using the TurboGrid software.

An extensive mesh study is performed to assess the effect of mesh parameters, which is explained later in Sec. V A. Here, for the sake of illustration, a zoomed view of the coarsest mesh (i.e., Level 1) that contains a total of 9.3×10^6 cells is shown in Fig. 4. The finer meshes utilize the same block topology and their illustration is not feasible due to extreme mesh density.

C. Temporal discretization scheme and time step

All the temporal derivatives in the transport equations are discretized using the implicit second-order backward scheme.[76] The time step is chosen as $\Delta t = 2 \times 10^{-5}$ s, which corresponds to a runner rotation of 0.1°. The blade passing frequency is calculated as $f_\mathrm{b} = z_\mathrm{b} f_\mathrm{n} = 155.3$ Hz, where z_b and f_n are the number of blades and the rotational frequency of the runner, respectively. Therefore, the time step frequency is two orders of magnitude larger than one of the highest frequencies that need to be resolved in the flow field. The average CFL number of the finest mesh (i.e., Level 4, more information provided in Sec. V A) oscillates around 0.1 throughout the simulation while 99.3% of the cells had a Courant number of below 1.

D. Divergence schemes

The divergence term in the momentum equation is discretized using a low-dissipation scheme, called `DESHybrid` in OpenFOAM, specially developed for DES simulations.[77,78] It is a blended convection discretization scheme that combines a low-dissipating scheme (usually second-order central, i.e., `linear`) with a diffusive scheme (usually second-order upwind, i,e., `linearUpwind`) to ensure the stability of the simulation while preserving accuracy. Accordingly, the face-centered value of the transported quantity ϕ is interpolated as

$$\phi_\mathrm{c} = (1 - \sigma_\mathrm{u})\phi_\mathrm{c} + \sigma_\mathrm{u}\phi_\mathrm{lu}, \tag{28}$$

where ϕ_c and ϕ_lu are the face-centered values through the central and second-order upwind scheme, respectively. σ_u is the blending factor and specifies the contribution of the second-order upwind scheme. σ_u

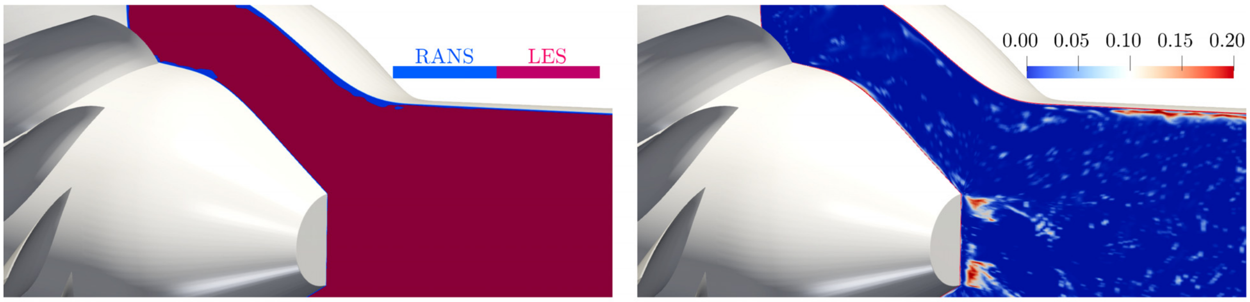

(a) LES (red) and RANS (blue) regions (b) Distribution of σ_u

FIG. 5. Illustration of (a) the LES and RANS regions and (b) the distribution of the blending factor (σ_u) of the `DESHybrid` convection scheme on the $x = 0$ plane of the finest mesh (Level 4).

is bounded by user-defined lower and upper values, i.e., $0 \leq \sigma_{\min} < \sigma_{\max} \leq 1$. σ_u tends to approach the lower limit in the LES region (which is usually the main region of interest) and the upper limit in the RANS and non-turbulent inviscid regions. In the current study, the σ_u limits are chosen as $\sigma_{\min} = 0$ and $\sigma_{\max} = 0.2$, meaning that the scheme switches to the full central in the highly resolved LES region while it contains a maximum of 20% contribution of the second-order upwind scheme in the non-resolved regions (e.g., very close to the walls). The blending factor σ_u is solution-dependent and varies in both time and space. It has an elaborate definition that is omitted here for brevity. Readers are referred to Spalart *et al.*[78] for the full formulation. Figure 5(a) displays the instantaneous distribution of the LES (red) and RANS (blue) regions in the test section close to the runner, while Fig. 5(b) shows the variation of σ_u at the same time step. It is seen that σ_u is mostly close to zero, and thus, the convection scheme is predominantly fully central, except for a thin layer close to the wall and also some other small regions that could be caused by the mesh quality (such as close to the runner crown, probably due to high aspect ratio cells). A comparison of the two figures indicates that the `DESHybrid` scheme does not simply work as a switch between the two connection schemes in the RANS and LES regions. Instead, it blends them in a way that strives for the highest accuracy while ensuring numerical stability.

The convection term in the transport equation of the turbulent viscosity is discretized using the TVD scheme `limitedLinear`[76] with a user-defined coefficient $k = 0.1$ that ensures low dissipation (with $k = 0$ the `limitedLinear` becomes the central differencing scheme).

E. Solution procedure

Pressure–velocity coupling is handled using the PIMPLE algorithm, which is a combination of the SIMPLE[79] (as outer correction loop) and the PISO[80] (as inner correction loop) pressure–velocity coupling algorithms. The consistent version of the SIMPLE algorithm, i.e., SIMPLEC[81] is utilized as the outer correction loop. At each time step, a maximum of eight outer correction loops is carried out with convergence residual criteria of 10^{-5} and 10^{-6} for p and U, respectively, which is achieved mostly within four outer correction loops. In each outer loop, three inner loops are performed. To ensure convergence of all explicit terms in the discretized equations, a non-orthogonal correction loop is performed in each inner correction. The pressure–velocity coupling algorithm ensures a physical pressure distribution through an implied implementation of the Rhie–Chow interpolation technique.[82]

The turbulence viscosity transport equation of the Spalart–Allmaras IDDES models is solved at the end of the final outer loop in each time step. Furthermore, the dynamic mesh calculations due to the solid-body rotation of the runner are conducted at the beginning of the first outer loop, and subsequently, the face fluxes are calculated relative to the mesh motion to satisfy mass the conservation.[83,84]

F. Boundary conditions

The inflow velocity boundary condition is computed through the divergence free synthetic eddy method (DFSEM),[85] i.e., the `turbulentDFSEMInlet` boundary condition in OpenFOAM. The boundary condition produces physically synthesized eddies at the boundary that are required for resolved simulations of turbulent flows (DES, LES, DNS). In order to set up the boundary condition, first a fully developed flow through a pipe with the same diameter and flow rate as the TSG inlet condition was computed through a steady RANS simulation. The resulting flow field distribution was utilized as the base profile for the `turbulentDFSEMInlet` boundary condition, and fluctuations generated through the synthesized eddies are added to impose a time-varying spatially non-uniform velocity distribution while ensuring a constant flow rate.

The inlet pressure is calculated based on a zero-gradient assumption. At the outlet boundary, the zero-gradient condition is imposed on U and $\tilde{\nu}$, while the pressure is assumed to be constant. Backflow is prevented at the outlet boundary by setting the velocity to zero at faces where the flux tends to be reversed.

A no-slip boundary condition is applied for the velocity at all walls, while turbulent viscosity is calculated using the OpenFOAM's wall function `nutUSpaldingWallFunction`. A zero-gradient assumption is applied on the wall pressure boundary condition.

The non-conformal mesh interfaces are coupled using the cyclic arbitrary mesh interface (`cyclicAMI`) boundary condition. This interface transfers the flow properties using a conservative interpolation based on an efficient strategy developed for general transport equations.[86,87]

G. Parallel processing

The numerical domain is decomposed with the scotch[88] decomposition method with uniform weights, ensuring load balance and minimizing the number of processor boundary interface faces. The inter-process information is exchanged using the message passing interface (MPI).[89] The simulation with the finest mesh of 54.7 × 10^6 cells is distributed on 50 compute nodes of an HPC cluster where each node has 32 cores and 96 GiB of RAM. Hence, the massively parallel computation is performed using 1600 CPU cores. The full simulation, including the time required to establish a statistically stationary flow field, takes around 27 days to complete. Hence, the total computational cost of the simulation with the finest mesh is 1.04 × 10^6 core hours.

V. RESULTS AND DISCUSSION

The results of the current study are presented and discussed in this section. First, the reliability of the DES simulation is verified (e.g., mesh study), and then, the results are validated against experimental data. Subsequently, the computed flow field through the resolved DES simulation is analyzed in detail. Finally, an in-depth DMD modal analysis is conducted, and its results are connected to the flow field study.

A. Verification and validation

TABLE I. Number of cells in different regions of each mesh.

Density	Struts	Guide vanes	Runner	Test section	Total
Level 1	1.7 × 10^6	1.4 × 10^6	1.5 × 10^6	4.6 × 10^6	9.3 × 10^6
Level 2	2.4 × 10^6	2.4 × 10^6	3.2 × 10^6	8.7 × 10^6	16.8 × 10^6
Level 3	4.1 × 10^6	5.2 × 10^6	6.8 × 10^6	15.6 × 10^6	31.6 × 10^6
Level 4	7.4 × 10^6	10.5 × 10^6	12.3 × 10^6	24.4 × 10^6	54.7 × 10^6

The mesh properties play a substantial role in resolved simulations of turbulent flows, such as DES simulations. Not only the switch between URANS and LES is affected by the mesh, but the level to which the turbulent kinetic energy is resolved in the LES region is heavily influenced by the mesh resolution. Therefore, the dependence on mesh resolution is assessed here through a systematic mesh study considering four computational meshes with different levels of density. The parameters of the meshes are presented in Table I. The coarsest mesh (Level 1) contains a total of 9.3 × 10^6 cells (displayed in Fig. 4), while the finest mesh (Level 4) consists of 54.7 × 10^6 cells.

The grid convergence method (GCI) method,[90] based on the Richardson extrapolation method,[91,92] is used for estimating the discretization error in the mesh study process. The detailed procedure is provided by Ref. 90. The following presents the results of the performed GCI mesh study on the velocity profiles on the measurement lines.

The variations of the time-averaged velocity components along the experimental velocity measurement lines W_0, W_1, and W_2 (see Fig. 3), obtained with the different computational meshes, are presented in Fig. 6. Inherited from the LDA technique that was used in

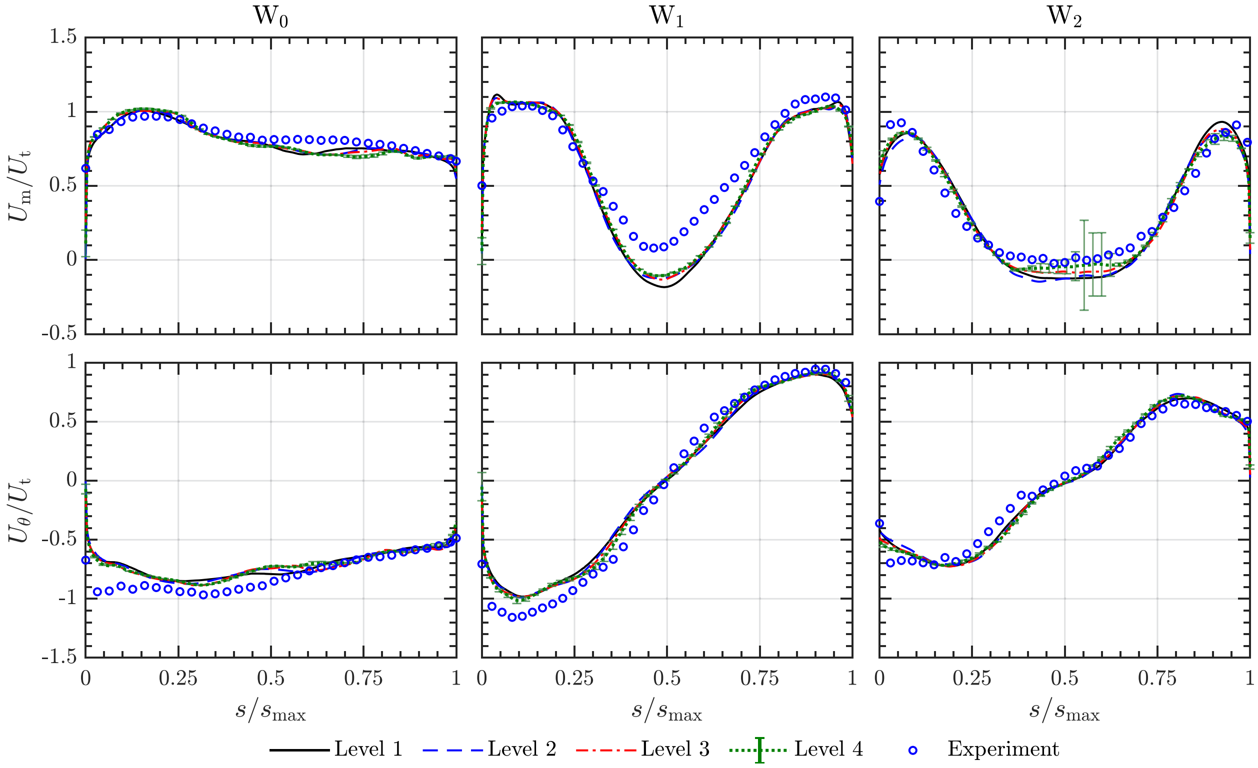

FIG. 6. Mean meridional and tangential velocity components along measurement lines W_0, W_1, and W_2, obtained with different meshes. The error bars show the discretization uncertainty calculated with the GCI method (in all plots, but only significant in one of them).

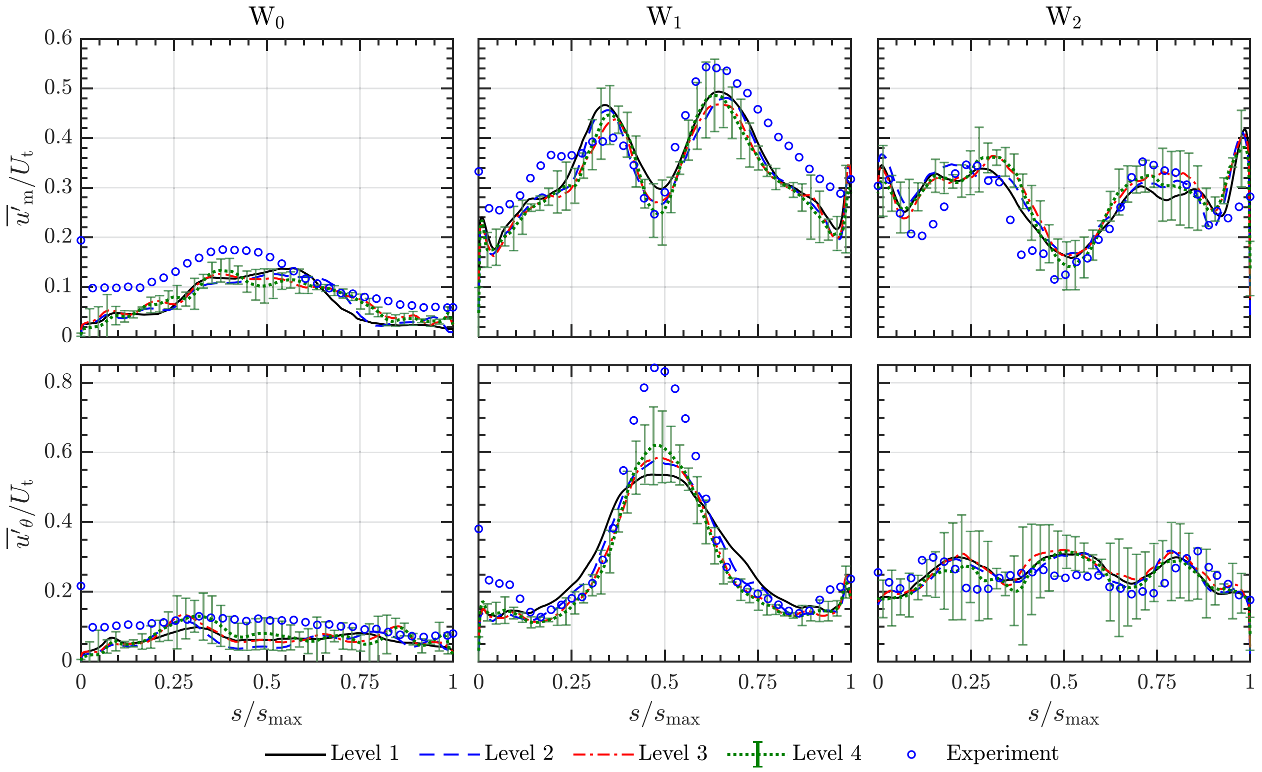

FIG. 7. RMS of resolved meridional and tangential fluctuating velocity components along measurement lines W$_0$, W$_1$, and W$_2$ obtained with different meshes. The error bars show the discretization uncertainty calculated with the GCI method.

the experimental investigation,[93] the meridional velocity (U_{m}) component is in the midplane ($x = 0$) and perpendicular to each measurement line, while the tangential velocity (U_θ) happens to be in the x direction (see Fig. 3). Both the numerical and experimental velocity profiles are normalized with the test section throat bulk velocity (U_{t}). Note that the discretization error is also estimated for the results of the finest mesh (Level 4) using the two coarser levels (Level 2 and 3), and the obtained GCI index values are presented as error bars in all figures (although only significant in one of them).

The meridional velocity component along W$_0$ indicates a slightly decreasing trend from shroud ($s = 0$) to hub ($s = s_{\max}$) in the experimental data, which is well-captured by the numerical results. It is worth mentioning that the arrows on the measurement lines in Fig. 3 indicate the direction of increasing curve length s. No major difference

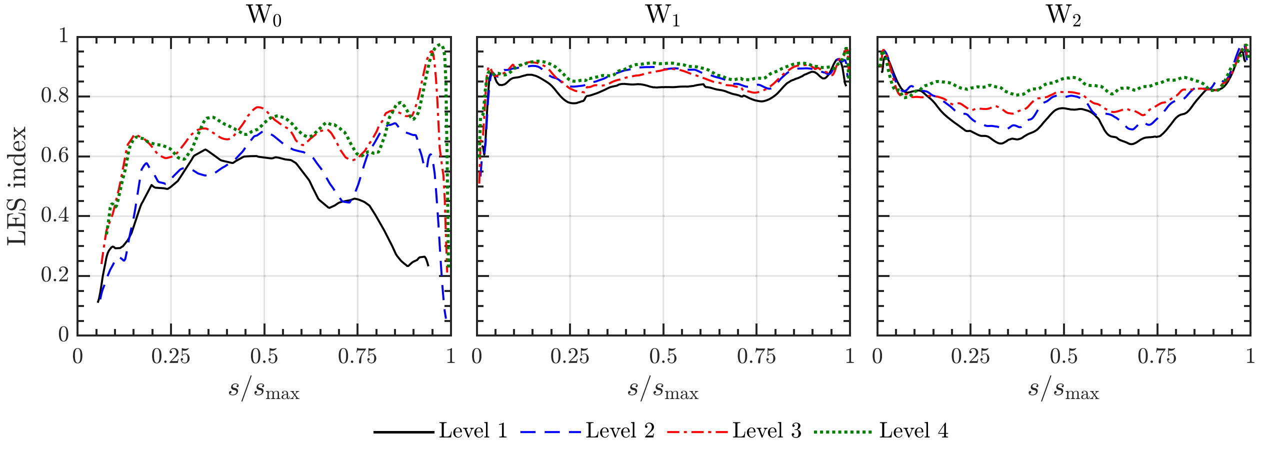

FIG. 8. Quality index of LES (relative resolved turbulence kinetic energy) along measurement lines W$_0$, W$_1$, and W$_2$.

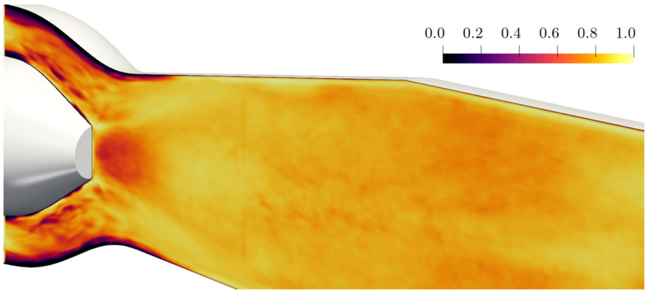

FIG. 9. Contour plot of the quality index of LES on the midplane ($x = 0$) of the test section.

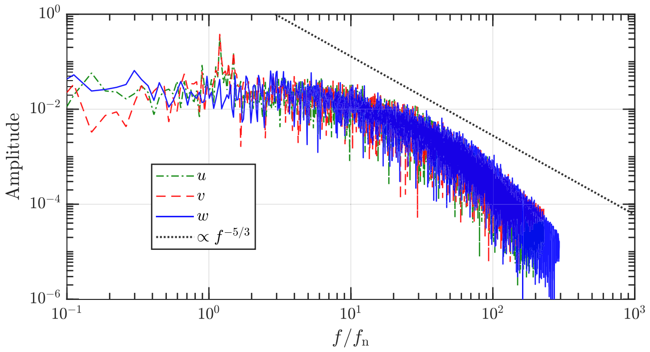

FIG. 10. Power spectral density (PSD) of the normalized velocity (u_i/U_t) compared to the Kolmogorov $-5/3$ slope.

is observed between the experimental and numerical profiles close to the shroud, showing that the simplification of not including the tip clearances in the simulations is acceptable. U_m shows a relatively symmetrical behavior along W_1 and W_2, with a significant decrease around the center of the lines due to the strong wake behind the runner hub. Compared to the measured data, the numerical results suggest a slightly larger reversed flow region behind the runner hub that has been extended beyond W_1, while the experimental data do not display any negative values at W_1. This is consistent with the previous numerical results reported in the literature.[64] The grid study results indicate an insignificant effect of mesh refinement on the mean velocity components as the three finest meshes (Levels 2, 3, and 4) produce somewhat similar profiles, except for the central region of W_2 line where the finest mesh (Level 4) gives the most accurate results predicting the smallest reversed flow region. The discretization error bars also show negligible uncertainty due to the spatial discretization, and the highest uncertainty in the normalized mean meridional velocity, attributed to the center of W_2, is ± 0.16.

The mean tangential velocity on W_0 indicates a nearly constant swirl along the curve length for both numerical and experimental data. However, the magnitude of experimental tangential velocity is slightly higher close to the shroud ($s = 0$). U_θ on both W_1 and W_2 lines exhibit a virtually anti-symmetric trend which indicates the swirling nature of the flow and is well predicted by the numerical simulations.

The root mean square (RMS) profiles of the resolved velocity fluctuations are presented in Fig. 7. In contrast to the mean velocity, the fluctuating terms are generally more challenging to accurately capture and heavily depend on the resolution of turbulent kinetic energy. The meridional ($\overline{u'_m}$) and tangential ($\overline{u'_\theta}$) components of the fluctuating velocity are under-predicted at W_0, which can be an indication of under-resolution of the turbulent flow that leads to under-prediction of turbulent kinetic energy at this location. The levels of fluctuating velocities are acceptable compared to the experimental data and follow similar trends along W_1 and W_2, except for the tangential component along W_1 which is under-predicted by the numerical results. This notable under-prediction of $\overline{u'_\theta}$ along W_1 can be attributed to the deficiencies of the IDDES model and is not significantly improved by the current substantial refinement of the mesh. Similar under-prediction and discrepancies between numerical and experimental fluctuating velocity were previously reported in the literature (Ref. 94). The mesh refinement significantly affects the resolution of the fluctuating velocity components, and the GCI method reveals an oscillatory convergence on several locations of each line. The error bars of the finest mesh show a notable uncertainty in the discretization error.

TABLE II. Quality parameters related to DES simulation for different meshes in the test section.

Density	$y^+_{\max}$	y^+_{mean}	LES region (%)	LES index (%)
Level 1	5.25	2.05	94.9	70.5
Level 2	4.13	1.61	94.6	71.1
Level 3	2.26	1.17	96.5	75.6
Level 4	2.56	0.98	97.4	81.2

The performance of an LES simulation can be assessed through the resolution of the turbulent kinetic energy. Resolving 80% of the turbulent kinetic energy can be considered "good" LES, while resolution above 95% is usually referred to DNS.[95] Therefore, the relative resolved turbulence kinetic energy, defined as

$$\frac{k_{\text{res}}}{k_{\text{tot}}} = \frac{k_{\text{res}}}{k_{\text{res}} + k_{\text{sgs}}} \tag{29}$$

can be considered as an index of quality for LES simulations. k_{res}, k_{sgs}, and k_{tot} represent the resolved, subgrid-scale (modeled), and total turbulent kinetic energies, respectively. Figure 8 displays the variation of this index along the measurement lines for different meshes. Note that the lines are not completely extended to the walls, meaning that the index is only shown in the LES region and the narrow URANS region close to the walls is excluded in these calculations. As expected, refining the mesh results in a higher turbulent kinetic energy. Level 4 is the only mesh that can resolve higher than 80% of the turbulent kinetic energy along both W_1 and W_2, where the RVR is formed and which is the main region of interest in this study. A contour plot of the LES quality index of the finest mesh (Level 4) on the midplane ($x = 0$) of the test section is shown in Fig. 9. It is seen that the index is generally higher than 80% at the conical part of the test section (the region of interest).

Table II displays important results related to the quality of the DES simulations and their LES resolutions in the test section. The average y^+ value is below one for the finest mesh, which shows that the boundary layer is sufficiently resolved in the RANS region. The LES region percentage shows how much of the total volume of the test section is resolved by LES. All the meshes primarily simulate the flow field through LES in the test section, and the URANS volume is generally less than 6% and occurs in a narrow region close to the walls [see Fig. 5(a) for visualization]. The LES index in the last column shows the volume-weighted average of the LES quality index in the test section. Level 4 is the only mesh that is achievable a higher value than 80%. Therefore, based on the presented mesh study, mesh Level 4 can be considered reliable for LES results in the test section, and thus, its results are chosen for the rest of the analysis (both flow and modal).

The adequacy of resolution of turbulent flow can be further explored by assessing the velocity fluctuations in the frequency space. As a well-established fact in the field, the fast Fourier transform (FFT) of a sufficiently resolved velocity within the inertial range adheres to the Kolmogorov slope, characterized by a power-law exponent of $-5/3$.[95]

To illustrate this, we present the FFT of velocity components along the midpoint of the MG0 line in Fig. 10. It is evident that the inertial range is effectively resolved, as confirmed by the line that follows the Kolmogorov slope of $f^{-5/3}$. This comparison adds further weight to the assertion that the LES region has been adequately resolved.

B. Analysis of CFD flow field

This section provides a detailed analysis of the CFD flow field in the investigated case study, as a foundation for the interpretations of the DMD results. Figure 11 presents the normalized pressure fluctuation at different pressure probes (at MG0, MG1, MG2, and MG3 levels close to the test section wall; see Fig. 3) compared to the experimental measurements.

The fluctuating part of the pressure is calculated by

$$p' = p - \bar{p}, \tag{30}$$

where $\bar{p}$ is the mean value. All the pressure values are normalized with the dynamic pressure of the test section throat, i.e.,

$$\tilde{p} = \frac{p}{p_{\mathrm{dyn,t}}} = \frac{p}{\frac{1}{2}\rho U_{\mathrm{t}}^2}, \tag{31}$$

where $p_{\mathrm{dyn,t}}$ and U_{t} represent the dynamic pressure and velocity magnitude at the test section throat, respectively. The time values are normalized with the period of the runner rotation (T), and the data are presented for five runner rotations.

Although the levels of pressure fluctuations are slightly overpredicted by the DES simulation, they are still in acceptable agreement with the measured data. High-frequency fluctuations are visible at MG0 [Fig. 11(a)] in the numerical results, superimposed on the high-amplitude low-frequency oscillations. The high-frequency fluctuations are attributed to the blade passing wakes and are strongest at MG0 which is the closest probe to the runner. Further downstream, at MG1–MG3 [Figs. 11(b)–11(d)], these fluctuations become less prominent. The experimental data do not show any trace of such high-frequency fluctuations, which is due to the low sampling frequency of the data measurement. The low-frequency oscillations are associated with the rotating vortex rope in the test section. Such oscillations are less distinguishable and ordered downstream of the test section (i.e., at MG3), which can be an indication of the disintegration of the vortex rope.

An FFT analysis of the fluctuating pressure signals is presented in Fig. 12. The frequencies are normalized with the runner rotation frequency ($f_{\mathrm{n}} = 1/T$). The strongest frequency in all subfigures represents the fundamental frequency of the RVR and is captured at $f/f_{\mathrm{n}} = 1.19$ in the numerical results. Although the frequency is marginally higher in the numerical results than in the experimental data, it matches the previous numerical results in the literature. As an

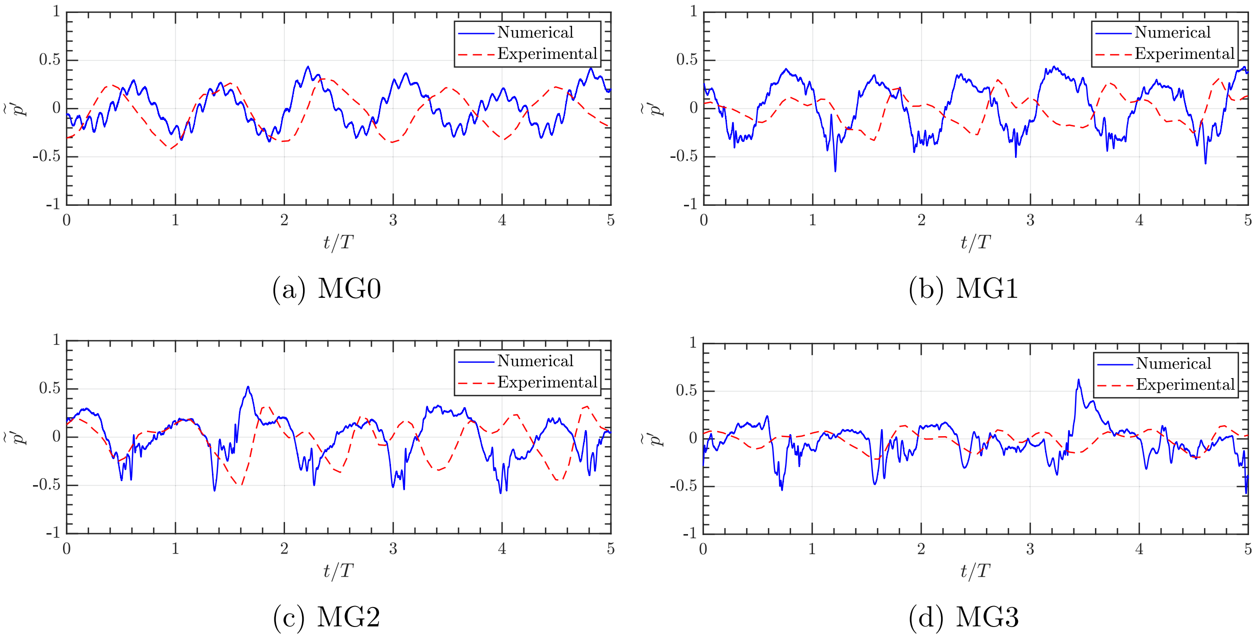

(a) MG0 (b) MG1

(c) MG2 (d) MG3

FIG. 11. Fluctuating pressure at different pressure probes.

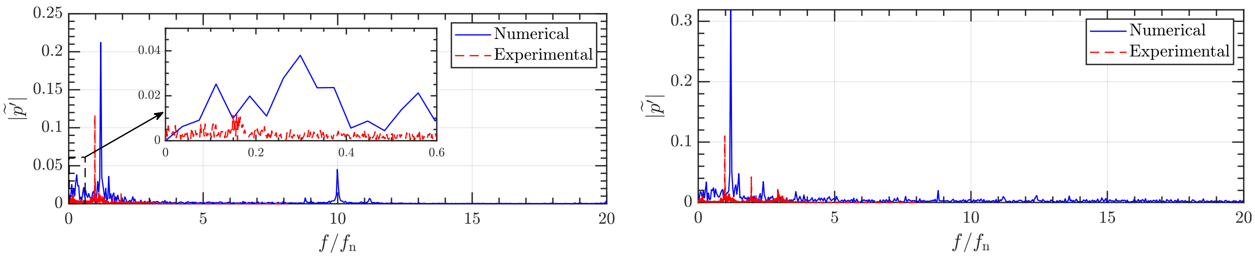

(a) MG0 (b) MG1

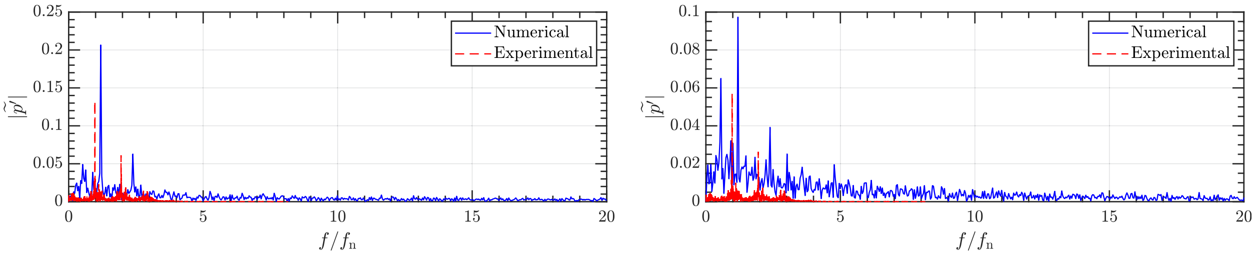

(c) MG2 (d) MG3

FIG. 12. FFT of the fluctuating pressure at different pressure probes.

example, Petit *et al.*[68] reported a normalized frequency of $f/f_\mathrm{n} = 1.21$ for the same flow configuration. The cause is a higher value of the flux of moment of momentum at the inlet of the test section, compared to the experimental data.

The excitation of the blade passing frequency at $f/f_\mathrm{n} = 10$ is visible at the MG0 probe [Fig. 12(a)]. However, the experimental sampling rate does not satisfy the Nyquist–Shannon[96,97] criterion to capture this high frequency, and the highest resolved normalized frequency in the measured data is $f/f_\mathrm{n} = 8.15$. That is the main reason for the absence of blade passing frequency in the experimental data [see both Figs. 11(a) and 12(a)]. Low-frequency excitations are observed across all probes (MG0–MG3) whose sources cannot be conclusively identified through mere FFT analysis of pressure probes. These observations will be investigated more in-depth throughout the article. Specifically, the first two probes (MG0 and MG1) illustrate an excitation at $f/f_\mathrm{n} = 0.29$ [see the zoomed-view in Fig. 12(a)], attributed to the axial oscillation of the vortex rope, recognized as the plunging effect, while MG3 and MG4 show excitation at slightly higher frequencies. The power spectrum of the pressure at MG3 [Fig. 12(d)] is more distributed over a broad range of frequencies, which can be explained by the disintegration of the vortex rope into a wide range of smaller structures with different frequencies.

The plunging and rotating effects of the vortex rope are investigated through a decomposition of the pressure signal. The self-induced instabilities in the conical section of the draft tube of hydraulic turbines generally consist of two types of oscillations, namely, rotating and plunging.[13,98] The plunging mode is attributed to the axial pulsations of the vortex rope and is sensed across the entire domain simultaneously, while the rotating mode is related to the precession of the vortex rope and is active locally in the cross section. Accordingly, the pressure signal decomposition can be performed using the unsteady signals of two different pressure probes that are positioned at the opposite sides of the draft tube cone as

$$\begin{aligned} p_\mathrm{sync} &= \frac{p_1 + p_2}{2}, \quad \text{Synchronous (plunging) component,} \\ p_\mathrm{async} &= \frac{p_1 - p_2}{2}, \quad \text{Asynchronous (rotating) component,} \end{aligned} \qquad (32)$$

where p_1 and p_2 represent the pressure signals of two opposing probes at the same cross section of the draft tube. p_sync specifies the pressure pulsations that are sensed by both signals simultaneously (plunging mode), while p_async characterizes the local pulsations that are recorded by each probe separately (rotating mode). In order to perform the decomposition, the pressures at the opposite location (with respect to the machine's axis) of each pressure level (MG0–MG3) are recorded in the numerical simulation, and subsequently, the synchronous and asynchronous components are computed at each level.

Figure 13 displays the FFT of both synchronous and asynchronous components for all pressure probes. The plots are presented in log scale for better representation over a wide range. The low frequency of $f/f_\mathrm{n} = 0.29$ is mainly excited at the synchronous component of the first two probes (MG0 and MG1), which represents the plunging mode, whereas the fundamental frequency of vortex rope, captured at $f/f_\mathrm{n} = 1.19$, is exclusively visible in the asynchronous component. The zoomed view of the asynchronous mode indicates that the strongest rotating mode is present at MG1 where the vortex rope is fully formed and its strength reduces downstream at MG2 and MG3 due to disintegration. However, the second harmonic of the vortex rope ($f/f_\mathrm{n} = 2.38$) and the runner blade passing frequency ($f/f_\mathrm{n} = 10$) are sensed at both opposing probes simultaneously and thus are seen in the synchronous mode.

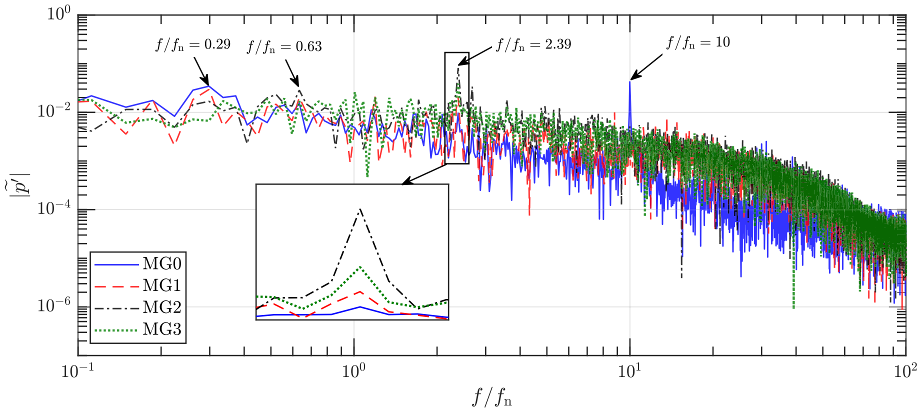

(a) Synchronous

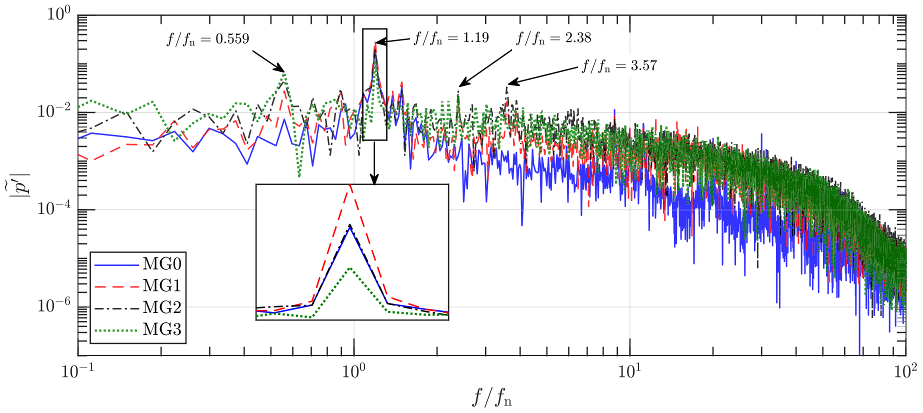

(b) Asynchronous

FIG. 13. FFT of synchronous and asynchronous components of the pressure at the probes.

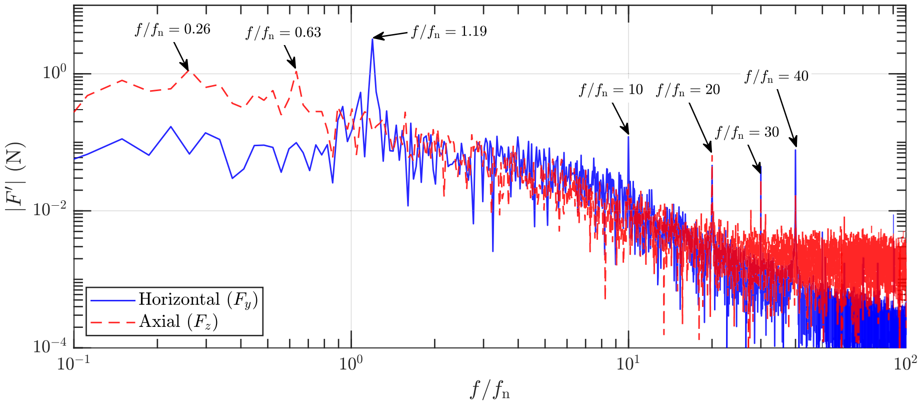

FIG. 14. FFT of the fluctuating horizontal (F'_y) and axial (F'_z) forces on the runner.

Two low-frequency excitations, namely, $f/f_\mathrm{n} = 0.63$ in the synchronous and $f/f_\mathrm{n} = 0.559$ in the asynchronous mode, are detected whose sources are not clear through the current analysis. However, through the modal analysis of DMD, it will be shown later that the frequencies are connected to boundary layer separation due to the adverse pressure gradient of the test section and the downstream reunited central core, respectively.

Performing a frequency analysis of the force components acting on the runner can offer additional insight into the coherent structures of the flow like the plunging and rotating modes, providing a physical explanation for these phenomena.

Figure 14 clarifies that the frequency of the plunging mode (which is detected at $f/f_\mathrm{n} = 0.26$ here) only appears in the axial force fluctuations. This establishes a clear connection between this frequency and the axial pulsations of the vortex rope. The small difference between the value of the plunging frequency in the pressure and force analysis might be due to insufficient sampling time. Considering a wider sampling time span provides more accurate frequency information due to the uncertainty principle.

Much like the synchronous mode in Fig. 13(a), the axial force exhibits a clear excitation at $f/f_{\mathrm{n}} = 0.63$. As explained, it will be shown through the DMD analysis that the coherent structures arising from the boundary layer separation on the outer wall of the test section encompass a similar frequency range.

The rotating mode frequency ($f/f_{\mathrm{n}} = 1.19$) is visible only in the horizontal fluctuations. The blade passing frequency ($f/f_{\mathrm{n}} = 10$) is mainly observed in the horizontal force, but its harmonics are clearly present in both the horizontal and axial forces. The amplitude of the high-frequency fluctuations ($f/f_{\mathrm{n}} > 10$) of the horizontal force decays linearly in the logarithmic scale, whereas it seems to remain at a constant level for the axial force and does not decay. Such high-frequency fluctuations are more likely generated by the small structures created by the disintegrated vortex rope downstream of the test section. Therefore, such high stochastic frequencies arising from small local flow structures predominantly impact the axial component of the force rather than the horizontal. This observation is compatible with our previous finding in a Francis turbine.[26]

The two horizontal components of the runner force, F_x and F_y, can be summed up in a vectorial manner to create the radial force. The value and direction of the radial force for five runner rotations are illustrated in Fig. 15. The change in the direction of this force is mainly driven by the vortex rope precession. Thereby, the radial force rotates more than five full rotations as the vortex rope fundamental frequency in this case is slightly higher than the runner rotation frequency ($f/f_{\mathrm{n}} = 1.19$). One can also see that the radial force magnitude and direction follow a rather chaotic pattern, which indicates the presence of smaller local structures that increase the complexity of the vortex rope precession.

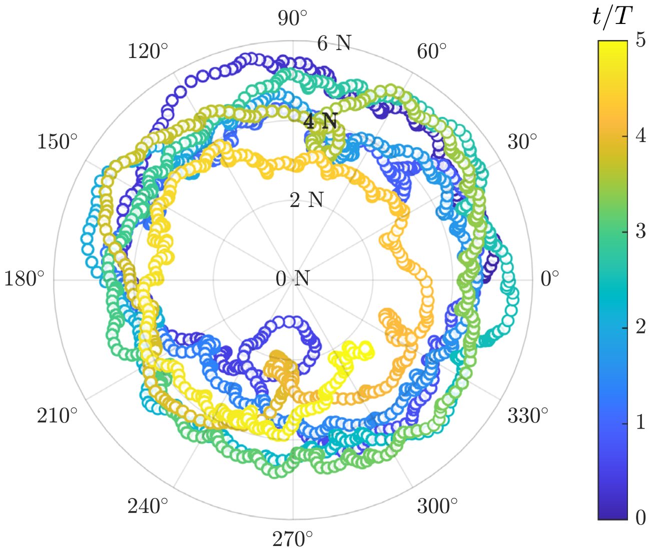

FIG. 15. Polar plot of runner radial force. The values on the radial axis indicate the magnitude of the radial force in N.

Here, we focus on examining the flow structures that develop within the test section. The λ_2 vortex identification technique[99] and vorticity magnitude contours are employed to detect and visually represent the vortical structures within the investigated test case. Figure 16(a) displays the iso-surface of $\lambda_2 = 3 \times 10^5\,\mathrm{s}^{-2}$ colored by axial velocity (U_z). Moreover, contours of vorticity magnitude (ω) on the test section midplane ($x = 0$) and four axial cross sections, namely, test section inlet, $z/D_{\mathrm{t}} = 1.5$, $z/D_{\mathrm{t}} = 2.5$, and $z/D_{\mathrm{t}} = 3.5$ are exhibited in Fig. 16(b). Note that similar planes are later used for the DMD analysis.

The wakes behind the runner blades' trailing edges form vortical structures that are transported with the flow. They seem to be mostly damped downstream by the convergent part of the test section, as no clear trace of such vortices is identified in the λ_2 iso-surface. However, vorticity contours still display weak remaining wakes at $z/D_{\mathrm{t}} = 1.5$.

A strong unified vortex rope is clearly observed, which is formed right behind the runner crown. The vortex rope is extended helically downstream and precesses in time. Considering the contours of the axial velocity, a large reversed flow region (negative axial velocity) is detected at the center of the test section. Therefore, as documented in the literature,[26] the vortex rope is helically wrapped around the stagnant region characterized by a reverse axial flow. The emergence of the vortex rope is known to be connected to the instability of the shear layer formed between the outer swirling flow and inner stagnant region that causes the rolling up of the interface, vortex breakdown, and the emergence of the vortex rope.

Shortly after the test section throat, the evolving boundary layer of the swirling outer region on the test section wall proves unable to withstand the pronounced adverse pressure gradient (APG) encountered in the divergent segment. This leads to instability within the boundary layer, resulting in boundary layer separation, as annotated in the figure.

The connection between the annotated vortical structure and the boundary layer separation becomes more apparent when examining the vorticity contours in Fig. 16(b) (see the annotated separated boundary layer). The expansion of the high vorticity region close to the diverging boundary of the test section, along with the detachment of high vorticity pockets in the form of vortex shedding, indicates the boundary separation phenomena due to the strong APG. The separation of the swirling outer region reduces the annulus space occupied by the high swirling flow, causing instability in the vortex rope and ultimately resulting in its disintegration.

Moving further downstream, the primary vortex rope structure loses stability and disintegrates, giving rise to a large number of disordered, local vortices that fluctuate across a wide spectrum of frequencies. A central slender reunited vortex core is formed after the disintegration of the vortex rope, which has been previously reported.[100]

C. Modal analysis

The modal analysis is conducted by employing dynamic mode decomposition on the velocity magnitude field from the finest mesh. This analysis necessitates temporal sampling of the results. Two critical parameters in this process are the DMD sampling frequency and the total sampled time, both of which demand careful consideration to ensure the accurate representation of the key physical phenomena and coherent structures.

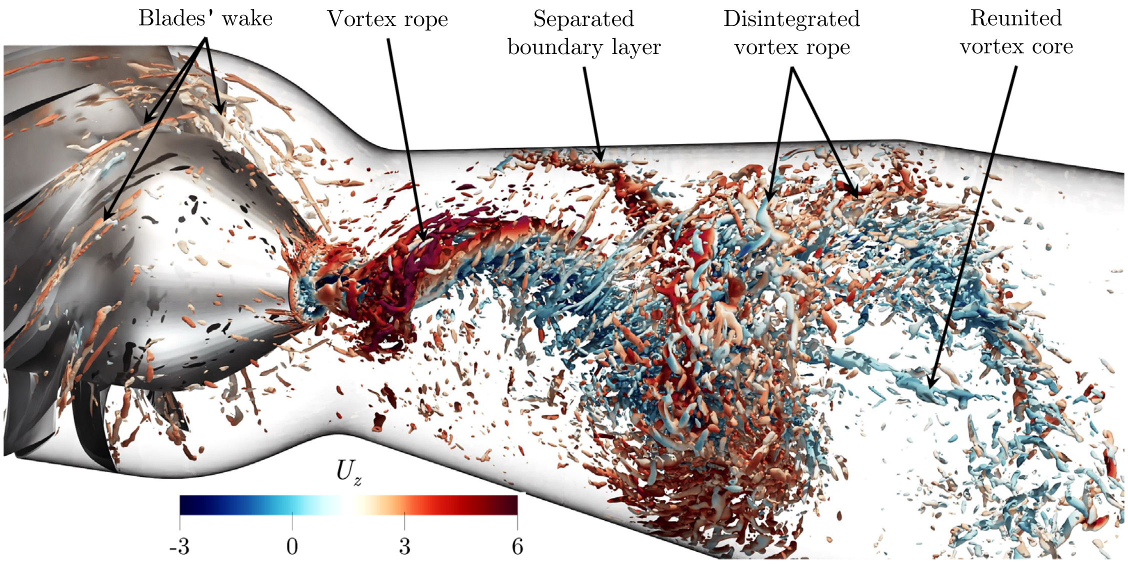

(a) Iso-surface of $\lambda_2 = 3 \times 10^5\ \mathrm{s}^{-2}$ colored by axial velocity (U_z)

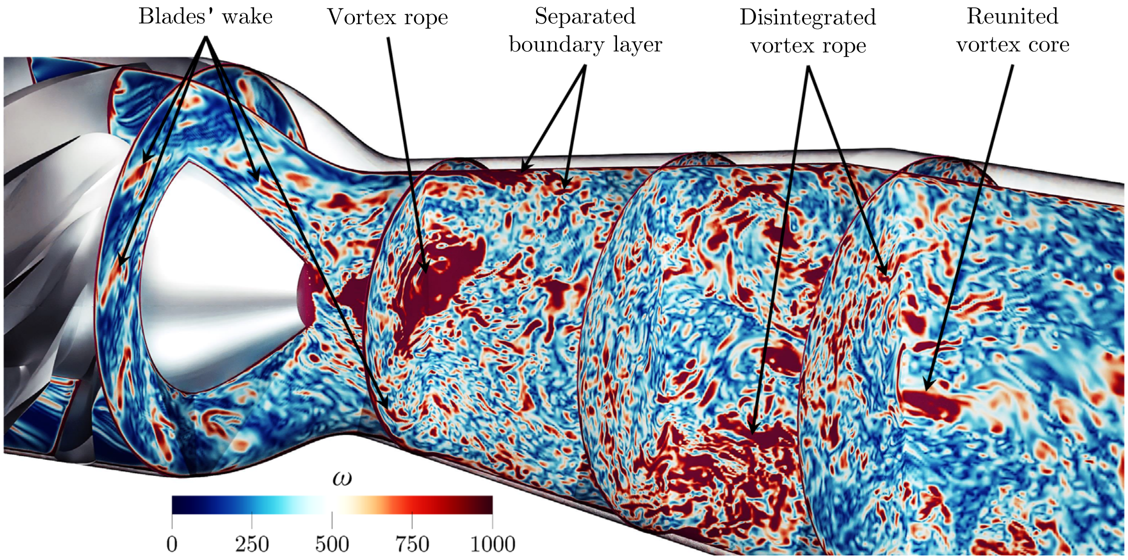

(b) Vorticity magnitude (ω) on the test section midplane ($x = 0$) and four axial cross sections, namely, test section inlet, $z/D_\mathrm{t} = 1.5$, $z/D_\mathrm{t} = 2.5$, and $z/D_\mathrm{t} = 3.5$

FIG. 16. Illustration of the instantaneous flow structures in the test section of the TSG through (a) $\lambda_2 = 3 \times 10^5\ \mathrm{s}^{-2}$ criterion and (b) vorticity magnitude contours.

1. Data sequence and DMD analysis

As discussed in Sec. V B, the flow field under investigation contains a wide spectrum of frequencies, ranging from the low-frequency plunging pulsations of the vortex rope at $f/f_\mathrm{n} = 0.29$ to the high-frequency runner blade wakes at $f/f_\mathrm{n} = 10$ and its harmonics. Consequently, to effectively capture the high-frequency coherent structures, the sampling interval must be significantly small. Conversely, the total sampling time needs to be sufficiently large to encompass multiple instances of the low-frequency phenomena. These two competing requirements make the modal analysis exceptionally challenging, particularly given the extremely fine computational mesh in use.

Here, the numerical results are recorded every 50 CFD time step ($\Delta t_\mathrm{CFD} = 2 \times 10^{-5}$ s), yielding a sampling time step of $\Delta t_\mathrm{CFD} = 10^{-3}$ s. Therefore, the DMD sampling frequency is $f_\mathrm{DMD}/f_\mathrm{n} = 65.2$, which according to the Nyquist–Shannon[96,97] criterion is sufficient to resolve the blade passing frequency up to its third harmonics. The total sampling time is chosen as $T_{\mathrm{DMD}} = 1$ s so that at least four periods of the coherent structures with the lowest frequency, corresponding to the plunging mode axial oscillation of the vortex rope, are recorded throughout the simulation. Therefore, a total of 1000 instantaneous snapshots of the flow field are stored during the CFD computations.

The DMD study is narrowed down to the test section (convergent–divergent pipe) of the computational domain since it is the main region of interest. However, capturing and analyzing all 1000 flow field snapshots on the computational mesh of the test section, comprising 24.4×10^6 cells, is not computationally viable. To overcome this challenge, the modal analysis is instead performed on multiple 2D planes, namely, one horizontal plane located at $x = 0$ and three axial planes at $z/D_{\mathrm{t}} = 1.5$, 2.5, and 3.5. The flow field of the fine mesh is sampled on the aforementioned planes with the same mesh resolution.

In addition to the 2D plane analysis, the DMD analysis is also performed on a three-dimensional mesh that is much coarser than the CFD mesh (roughly by a factor of 2.6 in all directions), consisting of only 1.32×10^6 cells. The numerical results are interpolated from the CFD mesh onto the DMD mesh at each DMD sampling time using a volume-weighted interpolation method.

Figure 17 provides a visual comparison between the instantaneous velocity magnitude on the test section midplane $(x = 0)$ obtained through the DES computations on the fine mesh and the interpolated results on the DMD mesh. As expected, some fine details of the flow field are lost during the interpolation procedure, but the main features of the flow are preserved. The interpolation effectively acts as a filter, removing small-scale variations in the flow. As a result of these procedures, a total of 380 GB of data were stored for the DMD analysis.

The DMD analysis starts with an SVD of the $\boldsymbol{X}_0$ matrix. The resulting non-zero singular values can be considered as a measure of the energy of each corresponding mode in the data matrix. Figure 18 shows the cumulative sum of singular values with respect to the total sum, representing the cumulative relative energy of the $\boldsymbol{X}_0$ POD modes. Notably, the cumulative energy does not exhibit the sharp rise observed in many other reduced-order modeling applications. In this case, it is not possible to pinpoint a mode index beyond which the energy contribution becomes negligible.

Consequently, accurately capturing the complex non-linear dynamics of the flow field through POD necessitates the inclusion of a significant portion of the modes. This phenomenon can be attributed to the chaotic and broadband nature of turbulent flows, in which all scales contribute to the overall flow energy. As shown in Fig. 9, a significant share of the turbulent kinetic energy is resolved through the DES simulation which yields a complex flow field with a wide range of energy spectrum. The same effect has been previously reported in the literature for modal analysis of Direct Numerical Simulation (DNS) of turbulent channel flow.[101]

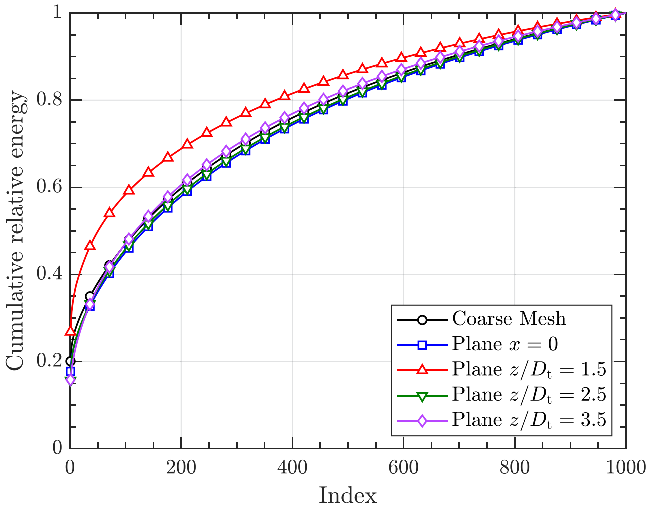

FIG. 18. Cumulative relative sum of non-zero singular values obtained through SVD of the $\boldsymbol{X}_0$ matrix.

Figure 18 also indicates that the plane at $z/D_{\mathrm{t}} = 1.5$ exhibits a more rapid convergence, implying that the flow field can be described using a smaller number of modes. This is attributed to the presence of organized flow oscillations generated by the coherent vortex rope at this location. In contrast, the other planes and the coarse mesh display lower cumulative energy due to the existence of resolved small-scale vortical structures resulting from the disintegration of the vortex rope. Using an arbitrary threshold of 80% for cumulative energy, it is found that the axial plane at $z/D_{\mathrm{t}} = 1.5$ requires only 370 modes to represent the flow field, while the remaining data sets necessitate a minimum of 450 modes.

2. Sparsity-promoting DMD performance

The sparsity-promoting DMD (SPDMD) algorithm is employed to selectively identify a subset of DMD modes that significantly

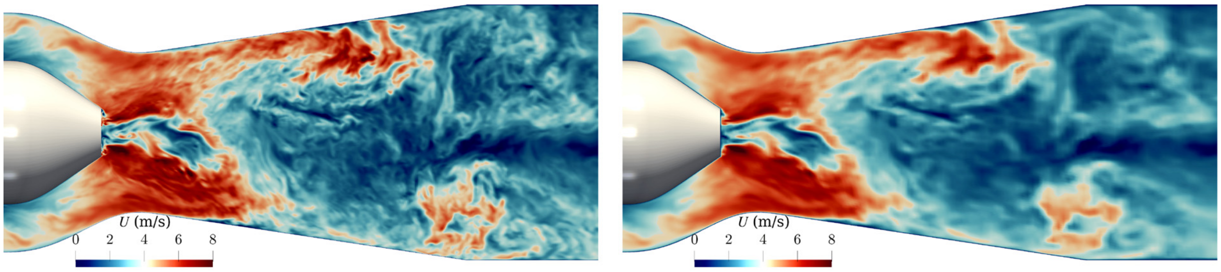

(a) DES Results (b) Interpolated on the DMD mesh

FIG. 17. Comparison of the CFD and interpolated results for the instantaneous velocity magnitude on the test section midplane $(x = 0)$.

influence the dynamics of the flow field. As discussed in Sec. II B, the regularization parameter of SPDMD, denoted as γ, controls the level of sparsity in the resulting DMD solution. Increasing this parameter reduces the number of DMD modes and increases sparsity, as illustrated in Fig. 19(a). It is important to note that a sparser solution may yield a less accurate representation of the field. To assess the accuracy of the recovered solution, the performance loss, as defined in Eq. (19), is used as a measure.

Figure 19(b) indicates that the first mode that can be considered as a representation of the time-averaged flow field contains a large share of the energy and can recover the solution with a maximum performance loss of 30%. Planes $z/D_\mathrm{t} = 2.5$ and 3.5 have the highest loss with the first few modes, while Plane $z/D_\mathrm{t} = 1.5$ has the most accurate representation of the dynamics. However, as the number of modes grows, the convergence rate of the axial planes increases, and their performance loss drops below the midplane curve which is explained by the fact that the axial planes have limited information about the entire flow field. In contrast, the test section midplane contains a full range of energy spectrum and has the lowest convergence rate.

The distribution of the real and imaginary parts of the eigenvalues of the $\tilde{\boldsymbol{A}}$ matrix (known as Ritz values) in the complex plane for the test section midplane ($x = 0$) is illustrated in Fig. 20. Here, only the midplane results are shown as the rest of the eigenvalue distributions demonstrate similar trends and do not provide extra information. The scatterplot represents the full DMD eigenvalues colored by their relative impact I [Eq. (24)]. The dashed line represents the unit circle of $|\lambda_j| = 1$.

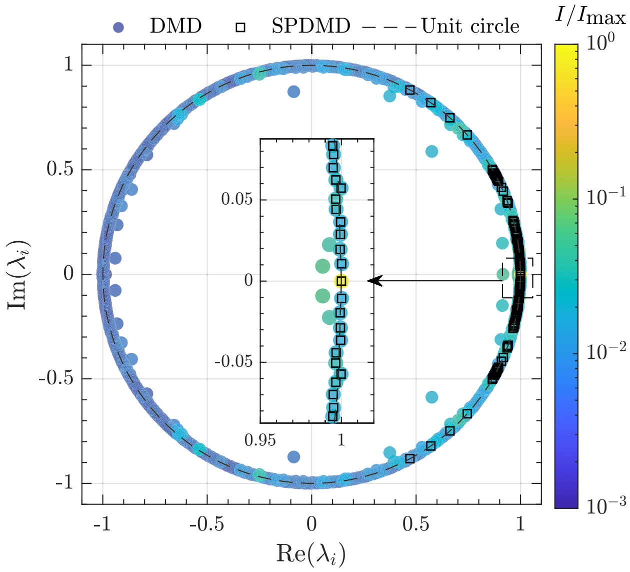

FIG. 20. Distribution of the complex eigenvalues, λ_j, for the midplane ($x = 0$) results.

The majority of DMD eigenvalues are closely situated near the unit circle ($|\lambda| = 1$), signifying that these modes exhibit a relatively stable behavior over time. This suggests that they neither significantly amplify nor decay. This observation aligns with the statistically stationary characteristics of the turbulent flow field under consideration, which involves persistent periodic instabilities. However, upon closer examination in the zoomed view, it becomes apparent that the magnitudes of some eigenvalues are not precisely equal to one, and some modes exhibit slight amplifying or decaying behaviors.

The squares indicate the first 111 modes recovered by the SPDMD algorithm using $\gamma = 6500$. The squares are not colored for better clarity as they have nearly similar levels of I as the full DMD eigenvalues. The SPDMD algorithm successfully identifies and recovers the most influential modes, offering a sparse solution in which the primary features of the flow are retained. Notably, none of the strongly damped modes ($|\lambda| < 1$) are included in this sparse solution.

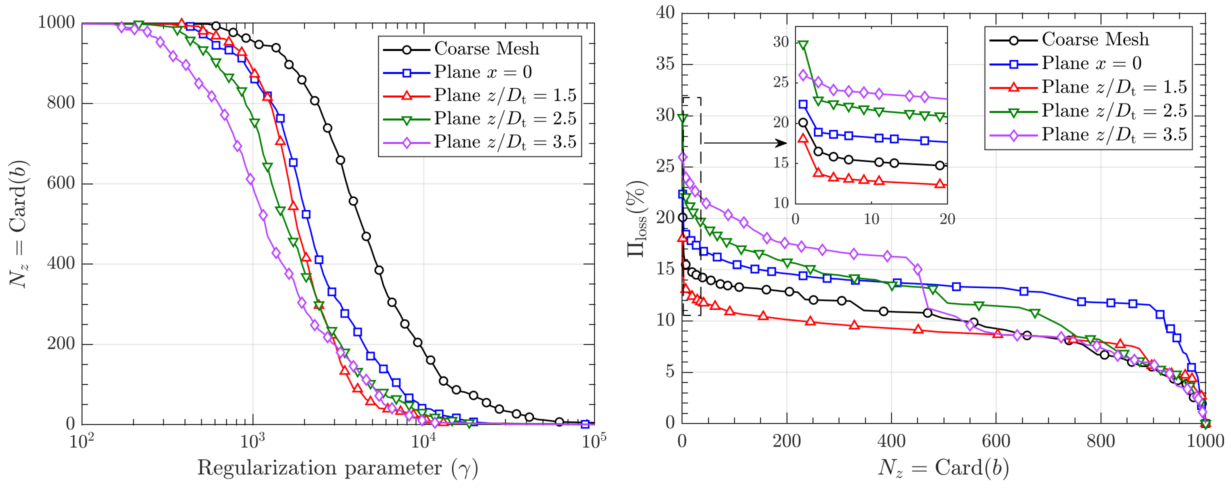

(a) Effect of γ on cardinality (b) Performance loss

FIG. 19. Performance of the SPDMD algorithm: (a) the effect of the regularization parameter γ on the cardinality (number of modes, i.e., sparsity) of the recovered DMD solution, and (b) variation of the performance loss $\Pi_\mathrm{loss}(\%)$ with the cardinality of the solution.

In DMD analysis, each mode contains an isolated frequency of the dynamical system. Figure 21 displays the dependence of the absolute value of the mode amplitude α_i, i.e., the contribution of the DMD mode to the initial condition, on the frequency of the mode. For the sake of clarity, only the frequencies up the blade passing frequency ($f/f_\mathrm{n} = 10$) are shown here. The full DMD results are compared to the recovered SPDMD modes with different sparsity levels.

Two non-oscillatory modes are identified precisely at $f/f_\mathrm{n} = 0$. However, when reconstructing these modes through the SPDMD algorithm, the one with the lower mode amplitude is primarily recovered, which might appear contradictory. However, it is important to note that α_i represents the mode amplitude of the initial condition ($\boldsymbol{x}_0$), whereas the complete contribution of the modes in time includes the powers of the eigenvalues of $\tilde{\boldsymbol{A}}$ [as shown in Eq. (12)]. The magnitude of the eigenvalue of the non-oscillatory mode recovered by SPDMD is $|\lambda| = 1.0$, while the other stationary mode has an eigenvalue of $|\lambda| = 0.916$. Therefore, only the recovered stationary mode persists in time, whereas the other mode decays relatively fast in time. In fact, this mode represents the mean flow field around which the flow dynamics oscillates.

The SPDMD does not select modes based on their amplitudes and is able to successfully recover the most influential modes by considering their total effect. Differences are observed between the mode amplitude of the full DMD modes compared to the recovered sparsity-promoting modes. This is because the SPDMD algorithm adjusts the amplitude of the preserved modes to provide an optimal solution to the problem in Eq. (21). Increasing the number of recovered modes (by decreasing the regularization parameter) reduces the discrepancies between the DMD and SPDMD modes' amplitudes. As expected, recovering all the modes with SPDMD results in exact amplitudes as the full DMD (not shown here for brevity).

3. Comparison of DMD and POD

To facilitate a comparative study, a POD analysis is conducted on the same data sequence, and the frequency contents of the POD modes are contrasted with the corresponding DMD results.

In Fig. 22, we analyze the frequency content of the first 12 DMD modes on the midplane ($x = 0$), which have been recovered by the sparsity-promoting algorithm. This analysis is carried out through an FFT of the real part of the modes' time dynamics. It is important to note that DMD modes come in pairs with positive and negative frequency values, and for the sake of the analysis, we only consider one mode from each pair. The obtained results are then compared to the corresponding values from the FFT of the time coefficients of the first 12 POD modes.

The FFT analysis of the DMD modes' coefficients reveals a single prominent peak for each mode. The DMD modes contain isolated frequencies that can be directly associated with distinct physical phenomena. In contrast, the POD modes exhibit a noticeable spectral leakage over a wide range of frequencies. While the amplitudes of the FFT of

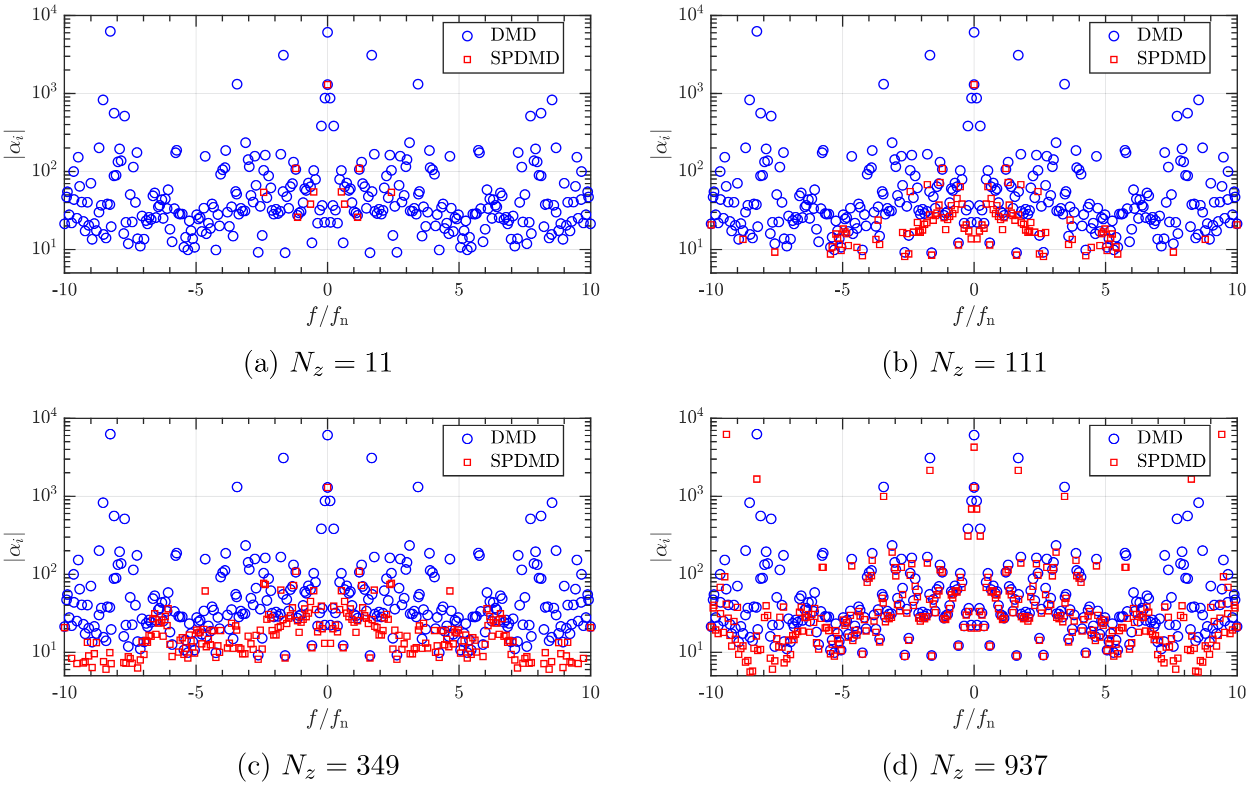

(a) $N_z = 11$ (b) $N_z = 111$

(c) $N_z = 349$ (d) $N_z = 937$

FIG. 21. Dependence of the absolute value of the mode amplitude α_i on the frequency of the mode. The full DMD results are compared to the recovered SPDMD values with different levels of sparsity.

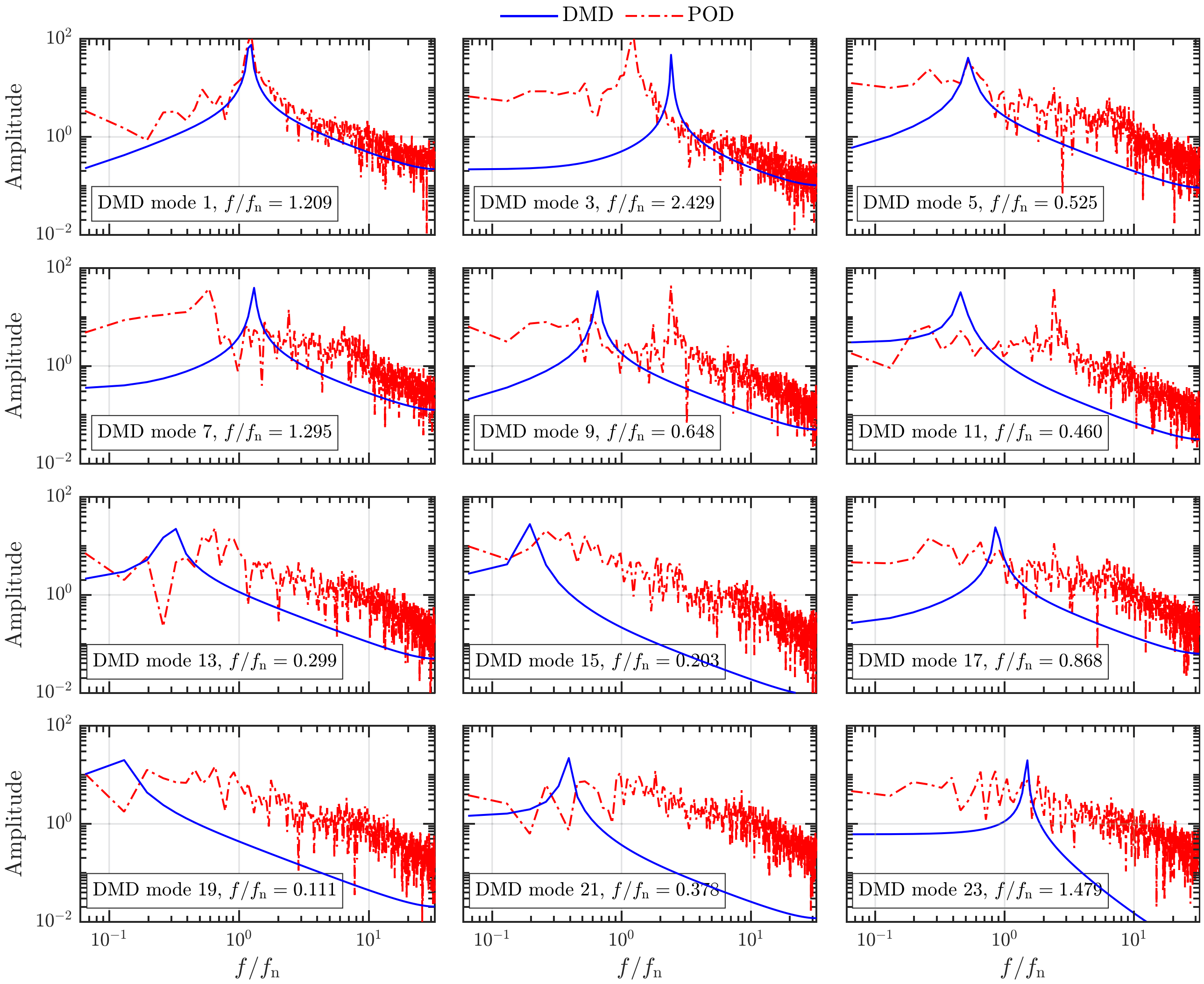

FIG. 22. A comparison between FFT analysis of time coefficients of DMD and POD modes of the midplane ($x = 0$) results.

POD coefficients may have peaks at fundamental frequencies (e.g., the vortex rope frequency), no individual POD mode can be linked to a single physical frequency. This distinction can be explained by the fact that POD modes are spatially orthogonal, meaning they capture spatial structures but not necessarily individual frequencies. On the other hand, DMD aims to provide eigenmodes that are temporally orthogonal,[46] allowing it to capture and isolate specific physical frequencies associated with coherent flow phenomena.

4. Coherent structures

The eigenmodes of the DMD algorithm provide a representation of the coherent structures within the flow field. This is achieved by isolating specific frequencies, enabling a clearer understanding of the underlying dynamics and patterns of the flow.

The real part of the first 18 SPDMD eigenmodes of the midplane ($x = 0$) is presented in Fig. 23 (Multimedia view). Mode 0 [Fig. 23(a)] is stationary ($f/f_n = 0$) and represents the time-averaged velocity magnitude of the flow field. The slight asymmetry observed in this mode may be attributed to the limited time span of the sampled data, and extending this span is expected to resolve it. The rest of the recovered modes are oscillatory with distinct frequencies that construct the non-linear dynamics of the system. The mode dynamics are reconstructed through the combination of mode pairs with their corresponding time coefficients.

An anti-correlated pattern is observed in Mode 1 [Fig. 23(b)], which propagates downstream indicating a precessing vortical structure. The mode encompasses the fundamental frequency of the vortex rope and represents the rotating (asynchronous) effect of this instability. The frequency is slightly overpredicted by 1.34% compared to the calculated frequency by FFT analysis of the fluctuating pressure and force signals in Sec. V B. The frequency of Mode 3 [Fig. 23(c)] is roughly two times larger than that of Mode 1 and similarly contains smaller anti-correlated patterns. Accordingly, Mode 3 is the second harmonic of Mode 1.

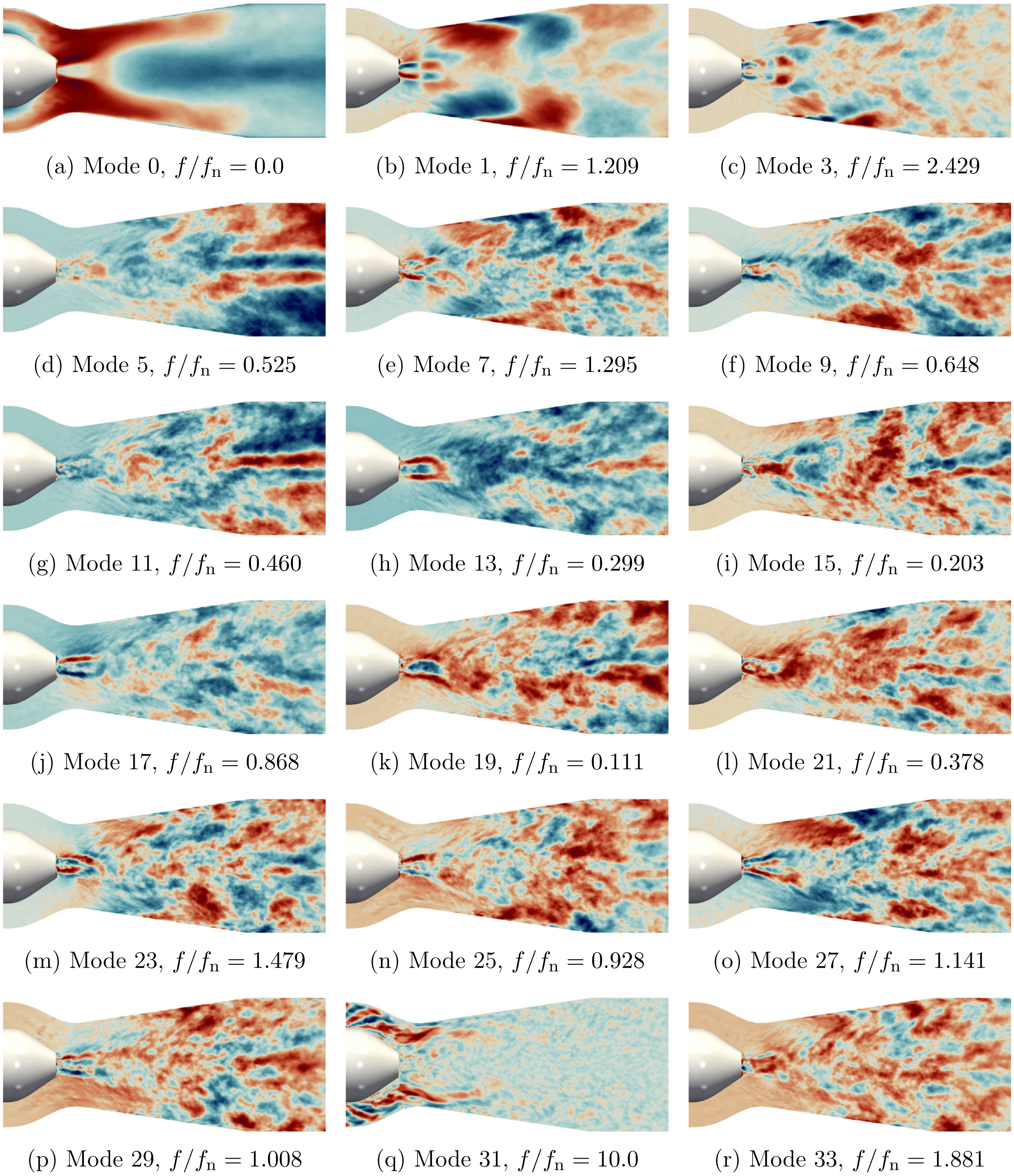
(a) Mode 0, $f/f_{\mathrm{n}} = 0.0$
(b) Mode 1, $f/f_{\mathrm{n}} = 1.209$
(c) Mode 3, $f/f_{\mathrm{n}} = 2.429$
(d) Mode 5, $f/f_{\mathrm{n}} = 0.525$
(e) Mode 7, $f/f_{\mathrm{n}} = 1.295$
(f) Mode 9, $f/f_{\mathrm{n}} = 0.648$
(g) Mode 11, $f/f_{\mathrm{n}} = 0.460$
(h) Mode 13, $f/f_{\mathrm{n}} = 0.299$
(i) Mode 15, $f/f_{\mathrm{n}} = 0.203$
(j) Mode 17, $f/f_{\mathrm{n}} = 0.868$
(k) Mode 19, $f/f_{\mathrm{n}} = 0.111$
(l) Mode 21, $f/f_{\mathrm{n}} = 0.378$
(m) Mode 23, $f/f_{\mathrm{n}} = 1.479$
(n) Mode 25, $f/f_{\mathrm{n}} = 0.928$
(o) Mode 27, $f/f_{\mathrm{n}} = 1.141$
(p) Mode 29, $f/f_{\mathrm{n}} = 1.008$
(q) Mode 31, $f/f_{\mathrm{n}} = 10.0$
(r) Mode 33, $f/f_{\mathrm{n}} = 1.881$

FIG. 23. Real part of the first 18 SPDMD modes of the midplane ($x = 0$) with their corresponding frequencies. Multimedia available online.

Modes 5 and 11 [Figs. 23(d) and 23(g), also see the corresponding videos] are primarily active in the downstream region of the test section where the vortex rope disintegrates into a wide range of local structures. Later, in Fig. 25, it is shown that the strongest non-stationary mode of Plane $z/D_{\mathrm{t}} = 3.5$ (which is placed around the same location) oscillates with a frequency in the similar range ($f/f_{\mathrm{n}} = 0.546$). The modes appear to partially represent the reunited vortex downstream of the test section, as described in Fig. 16(a).

A distinct anti-correlated pattern is prominently evident in the central region downstream of both modes, extending toward the outlet, that can express a central oscillating vortex.

A similar frequency peak was previously noted in the fluctuations of the asynchronous pressure mode [see Fig. 13(b)]. The current modal analysis has made it clear that these fluctuations are connected to the downstream reunited vortex. Considering the earlier FFT analysis in Fig. 13 and the fact that a similar frequency was observed only in the asynchronous component, it can be concluded that this mode represents the rotation of the downstream reunited vortex.

The boundary layer separation phenomena due to the strong APG, depicted in Fig. 16, appears to be represented by Mode 9 at $f/f_\mathrm{n} = 0.65$ [Fig. 23(f)]. The highest values of this mode align with the location of the separated flow region near the outer wall of the test section. Again, a rather similar frequency was previously observed to excite the synchronous pressure mode [Fig. 13(a)] and the axial force on the runner (Fig. 14). Hence, we can draw the conclusion that boundary layer separation induces axial oscillations at $f/f_\mathrm{n} = 0.65$. This discovery is attainable only through a combined DMD and flow analysis.

Mode 7 seems to be the harmonic of Mode 9, as its frequency is a whole number multiple of the original frequency. Mode 17 [Fig. 23(j)] appears to be associated with the vortex shedding phenomenon resulting from the flow separation behind the runner crown. Strong anti-correlated patterns are clearly visible behind the crown. The video depicting the mode's dynamics also demonstrates an oscillatory shedding-type behavior behind the runner.

Modes 13, 15, 19, and 21 [Figs. 23(h), 23(i), 23(k), and 23(l)] are low-frequency modes that oscillate with frequencies consistent with the range of the plunging (synchronous) effect. These modes feature a high-velocity oscillation region located directly behind the runner crown that does not alternate in the radial direction (as opposed to the rotating mode) and predominantly moves in the axial direction. The accompanying videos provide a distinct visualization of pronounced pulsations in the velocity magnitude in the axial direction behind the runner.

Mode 31 [Fig. 23(q)] has the same frequency as the runner blade passing frequency ($f/f_\mathrm{n} = 10$) and is attributed to the wakes behind the trailing edges of the runner blades. The mode is primarily active in the convergent region of the test section and is largely damped downstream of the throat. The observation is consistent with the purpose of the special design of the swirl generator, in which the convergent part was originally designed to eliminate the runner trailing edge wakes and decouple the vortex rope from upstream flow phenomena.[64]

The real part of the first 16 SPDMD modes of the axial cross sections, i.e., Planes $z/D_\mathrm{t} = 1.5$ and $z/D_\mathrm{t} = 3.5$, is illustrated in Figs. 24 (Multimedia view) and 25 (Multimedia view), respectively. Similar to the midplane, the strongest oscillatory mode of Plane $z/D_\mathrm{t} = 1.5$ [Mode 1 in Fig. 24(b)] corresponds to the rotating mode of the vortex rope where a helical vortex structure is observed.

Modes 3 and 13 [Figs. 24(c) and 24(h)] represent the second and third harmonics of the Mode 1, featuring two and three smaller helical structures, respectively. Also, their frequency corresponds to the whole number multiples of the vortex rope fundamental frequency. Visualization of the modes and their corresponding frequencies indicate that Modes 7, 9, 15, 19, and 23 also correspond to the rotating effect of the vortex and its harmonics and likely their interaction with other low-frequency phenomena.

Strong plunging effects are observed in Modes 5, 11, 21, and 29. Once again, it is seen that the plunging modes are nearly axisymmetric and do not show any sign of rotation, which is consistent with our observation on axial oscillating of the plunging mode in Fig. 23.

Mode 25 [Fig. 24(n)] exposes the runner blade trailing edge wakes with the blade passing frequency ($f/f_\mathrm{n} = 10$). Additionally, distinct eigenmodes representing linear combinations of the blade passing frequency with the vortex rope frequency, namely $(f_1 - f_2)/f_\mathrm{n} = 8.780$ and $(f_1 + f_2)/f_\mathrm{n} = 12.213$, are observed in Modes 17 and 27 [Figs. 24(j) and 24(o)], respectively.

Plane $z/D_\mathrm{t} = 3.5$ is situated in a region where the vortex rope is no longer integrated as a whole but has fragmented into smaller structures. Consequently, the most dominant non-stationary mode (Mode 1 in Fig. 25) oscillates at a frequency of $f/f_\mathrm{n} = 0.546$. Interestingly, a similar frequency range was observed in the eigenmodes of the midplane ($x = 0$), mainly occurring downstream of the test section. This mode likely represents the reformation of the central vortex after the disintegration of the vortex rope. The FFT analysis of the horizontal force components (e.g., F_y) acting on the test section walls also exhibits the highest peak at a similar frequency, consistent with the current observation (the results are not shown here for conciseness).

In plane $z/D_\mathrm{t} = 3.5$, Mode 3 exhibits the frequency closest to the vortex rope, even though its contours do not depict an integrated helical structure. Unlike the upstream plane ($z/D_\mathrm{t} = 1.5$), most modes in the downstream plane display a more chaotic structure. This chaotic behavior is a consequence of the disintegration of the vortex rope into a broad spectrum of stochastic frequencies that are resolved through the DES simulation.

5. Data reconstruction and prediction of future

Having obtained the DMD eigenmodes and their corresponding time dynamics, it becomes feasible to reconstruct the flow field to compare with the original data sequence and even predict the future that was not computed by CFD or measured in the experiment. Figure 26 presents the instantaneous SPDMD reconstructed velocity magnitude on the test section midplane ($x = 0$) at the final time step ($t = 1$ s) of the analyzed time span. Different levels of SPDMD sparsity are used to reconstruct the field. Their corresponding relative errors are also computed with respect to the CFD results, i.e., $|U_\mathrm{CFD} - U_\mathrm{SPDMD}|/U_\mathrm{t} \times 100$.

Considering only the first three eigenmodes, i.e., the time-averaged flow field and the mode pair representing the processing vortex rope [the modes were previously shown in Figs. 23(a) and 23(b)], the main dynamics of the flow field, i.e., processing vortex rope is captured [see Fig. 26(a)]. However, the reconstructed field is overwhelmingly smooth and simplified and lacks all the resolved local structures and eddies that contribute to the overall flow. The relative error is remarkable, especially downstream of the test section where the vortex rope is collapsed into small local structures [Fig. 26(d)]. As expected, to reconstruct fine details of the flow field and capture local eddies, more DMD modes are required. Increasing the number of modes and employing more than half of them ($N_z = 524$) results in an accurate reconstruction of the field with a negligible relative error [Figs. 26(c) and 26(f)]. The resulting field of the full DMD calculation is exactly as the reference data with a relative error of nearly zero everywhere (not shown here).

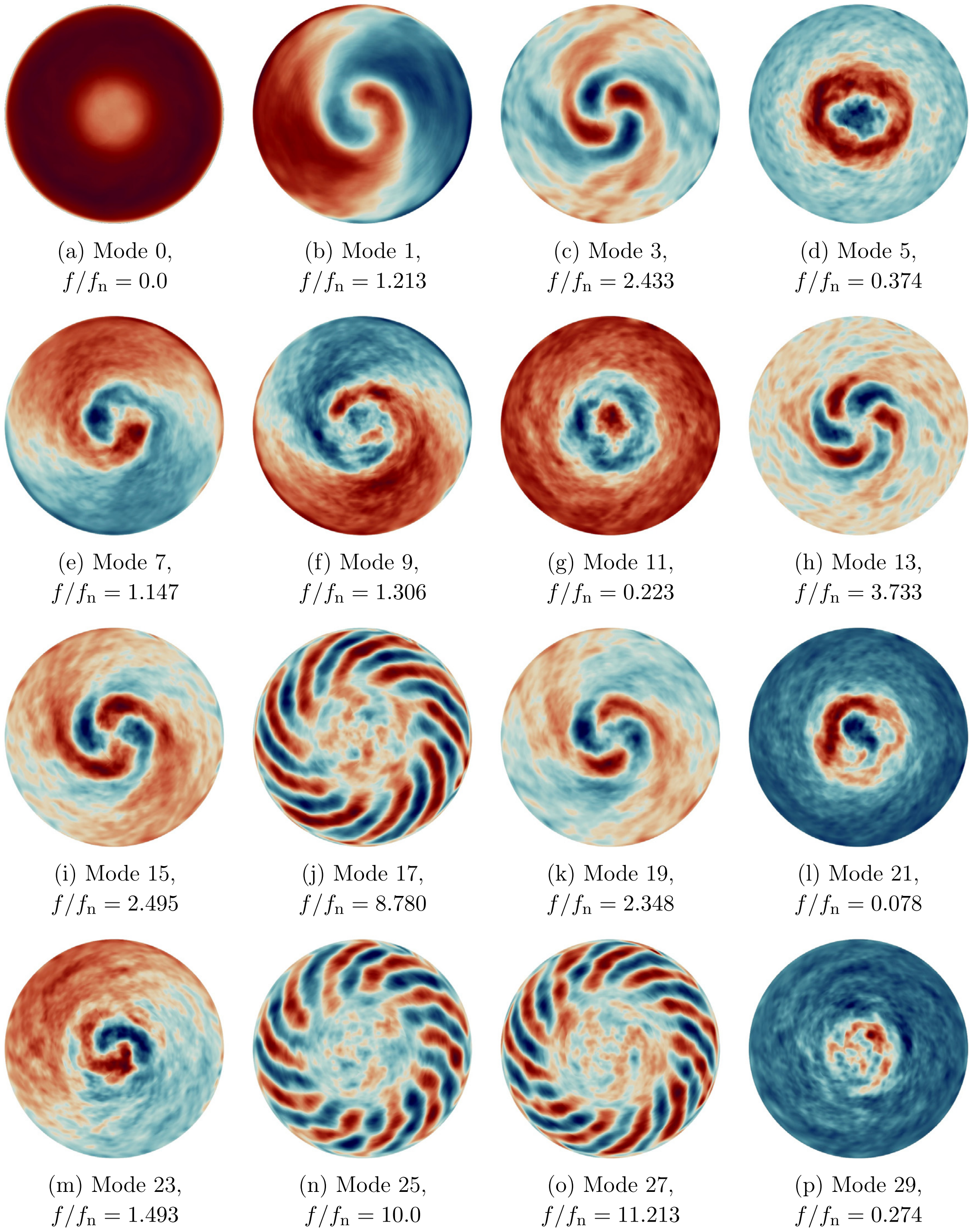

FIG. 24. Real part of the first 16 SPDMD modes of Plane $z/D_\mathrm{t} = 1.5$ with their corresponding frequencies. Multimedia available online.

The time-averaged relative error of the velocity magnitude, reconstructed with different sparsity levels, is presented in Fig. 27. The midplane results elucidate that the maximum average error occurs right behind the hub cone where chaotic local structures due to separated flow are resolved (see midplane and $z/D_\mathrm{t} = 1.5$ results). Inevitably, such fine details cannot be reconstructed only by considering the fundamental eigenmodes. In addition, the error increases close to the test section walls, where the flow separates. As seen previously, the flow separation

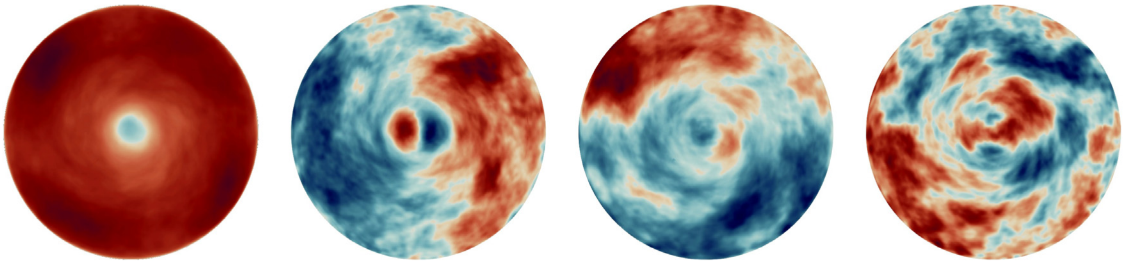

(a) Mode 0, $f/f_{\rm n} = 0.0$ (b) Mode 1, $f/f_{\rm n} = 0.546$ (c) Mode 3, $f/f_{\rm n} = 1.236$ (d) Mode 5, $f/f_{\rm n} = 1.089$

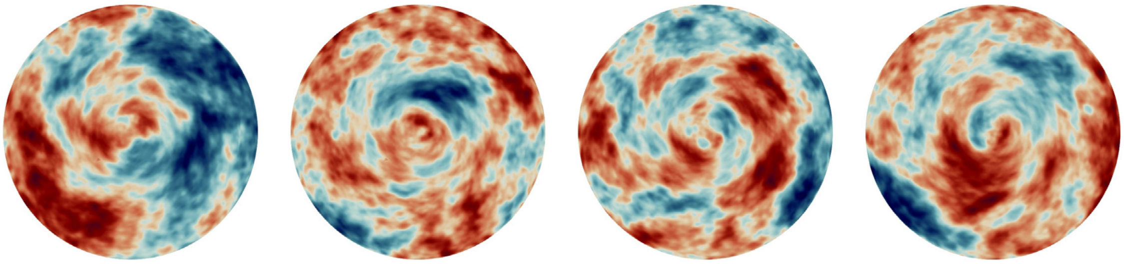

(e) Mode 7, $f/f_{\rm n} = 1.156$ (f) Mode 9, $f/f_{\rm n} = 0.504$ (g) Mode 11, $f/f_{\rm n} = 1.883$ (h) Mode 13, $f/f_{\rm n} = 0.613$

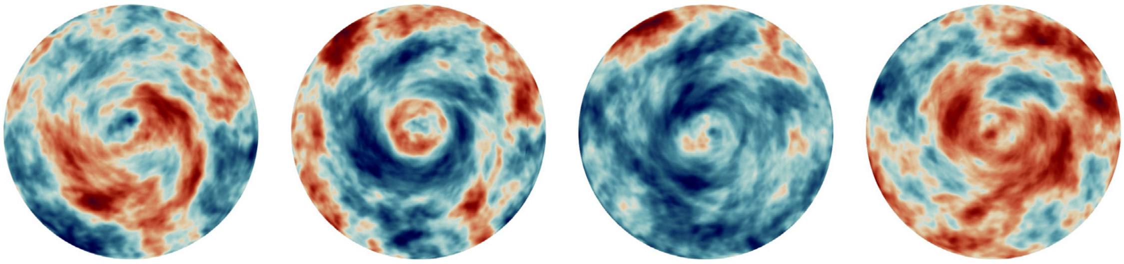

(i) Mode 15, $f/f_{\rm n} = 0.161$ (j) Mode 17, $f/f_{\rm n} = 0.426$ (k) Mode 19, $f/f_{\rm n} = 0.848$ (l) Mode 21, $f/f_{\rm n} = 1.321$

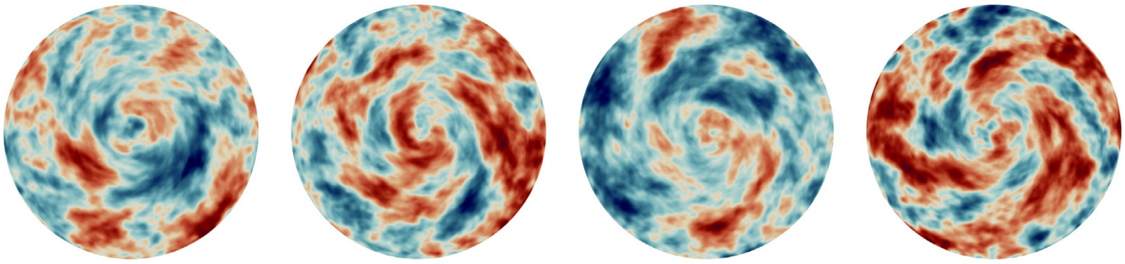

(m) Mode 23, $f/f_{\rm n} = 1.424$ (n) Mode 25, $f/f_{\rm n} = 0.247$ (o) Mode 27, $f/f_{\rm n} = 0.319$ (p) Mode 29, $f/f_{\rm n} = 1.982$

FIG. 25. Real part of the first 16 SPDMD modes of Plane $z/D_{\rm t} = 3.5$ with their corresponding frequencies. Multimedia available online.

phenomenon is represented by distinct modes and their consideration is essential for accurate reconstruction of the separated region.

The reconstructed and predicted fields are further studied by extracting and comparing them at four probes on the test section midplane shown in Fig. 28. The location of the probes is illustrated in the top right corner of the figure. Here, only the full DMD results are displayed. As seen in the previous figure, the full DMD reconstructed velocity, at $t \leq 1$ s, precisely matches the original data for all the

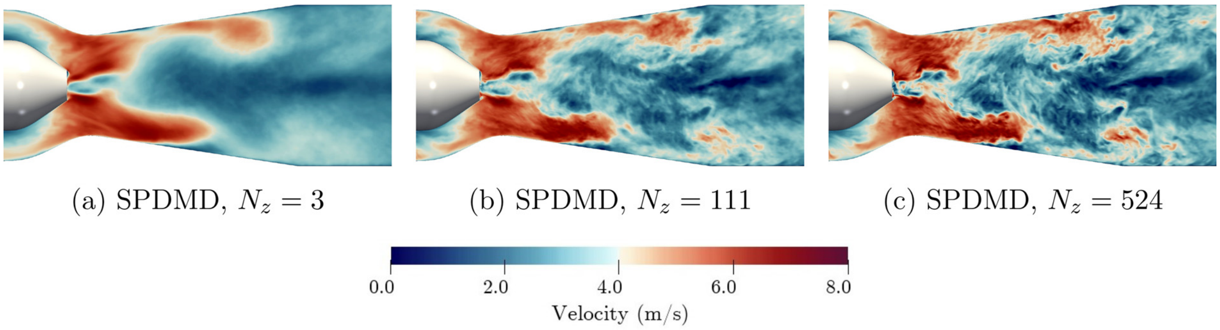

(a) SPDMD, $N_z = 3$ (b) SPDMD, $N_z = 111$ (c) SPDMD, $N_z = 524$

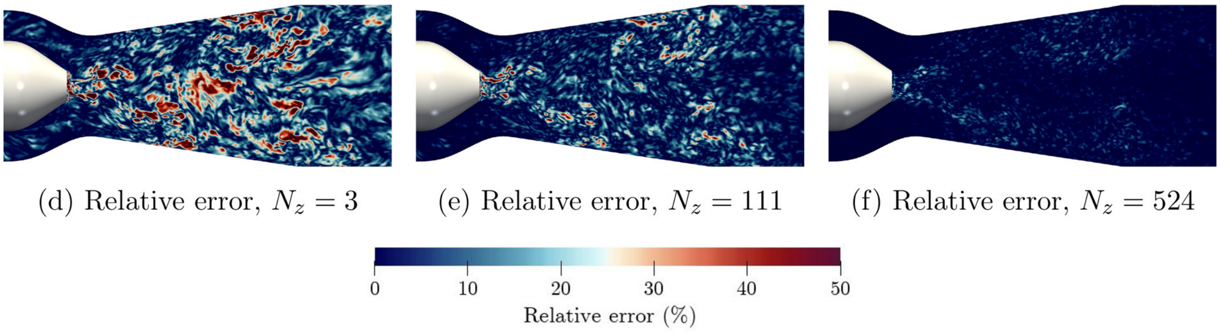

(d) Relative error, $N_z = 3$ (e) Relative error, $N_z = 111$ (f) Relative error, $N_z = 524$

FIG. 26. SPDMD reconstructed velocity magnitude field on the midplane ($x = 0$) at $t = 1$ s using different levels of sparsity and their corresponding relative errors.

probes. However, the modal analysis generally fails to predict the future ($t > 1$ s) with an acceptable level of accuracy. The chaotic nature of the resolved turbulent flow field, characterized by a wide range of frequencies, makes prediction of the future through modal analysis exceptionally difficult.

Another possible explanation for the lack of accurate prediction of the future could be the settings of the current DMD analysis. On the one hand, the DMD sampling frequency, set at every 50 CFD time steps, may cause information loss. With this frequency, at most 1000 DMD modes can be recovered (equivalent to the number of considered time steps). Utilizing all the CFD time steps could have generated 50 000 modes.

On the other hand, the analysis is carried out on a few 2D planes rather than the complete 3D CFD mesh. Hence, the DMD model has only access to the local information. It is known that the dynamics of turbulent eddies extend to all dimensions and analyzing local planes may not provide a comprehensive picture of the physics. Performing a DMD analysis on the entire CFD dataset (both in time and space) has the potential to enhance the precision of predictions of the future for this intricate system. Nonetheless, this computationally intensive analysis remains beyond the scope and feasibility of our current study.

Still, it is important to acknowledge that the classical DMD algorithm may inherently fall short in accurately describing and predicting the behavior of this complex non-linear system. As explained in Sec. II, DMD strives to provide a linear approximation of non-linear dynamical systems. Exploring more sophisticated alternatives, such as high order DMD (HODMD[102]) and spectral POD (SPOD[103]), might offer a more suitable modeling solution. This requires further investigation in the future.

In Fig. 28, Probe 1 is positioned upstream of the vortex rope, and its behavior is predominantly influenced by the runner's revolutions and the wakes generated behind the trailing edges of the blades. The high-frequency oscillations observed in the Probe 1 data correspond to the blade passing frequency. The presence of a well-organized periodic flow makes future prediction more feasible, leading to an adequate level of accuracy in velocity prediction.

Probes 2 and 3 are located further downstream in the region where the flow field is significantly influenced by the rotation of the vortex rope. Probe 2 can still detect the rotor blades and exhibits both high-frequency fluctuations caused by the wakes from the blades and low-frequency pulsations from the vortex rope. In contrast, Probe 3 primarily displays large oscillations related to the vortex rope. The full DMD analysis has accurately predicted the main trends in velocity variations for both probes, which are influenced by the coherent structures, with an acceptable level of accuracy. However, the DMD prediction does not accurately capture the finer details generated by the local turbulent eddies.

Probe 4 is positioned further downstream along the machine's axis, where the vortex rope has disintegrated. The chaotic velocity fluctuations at this probe are primarily caused by the presence of fine local turbulent structures that the DMD analysis struggles to accurately predict. Consequently, the modal analysis data are in complete disagreement with the CFD solution.

VI. SUMMARY AND CONCLUSION

The sparsity-promoting dynamic mode decomposition (SPDMD) algorithm was employed to conduct an intricate modal analysis of the vortex rope instability within a swirl generator. This

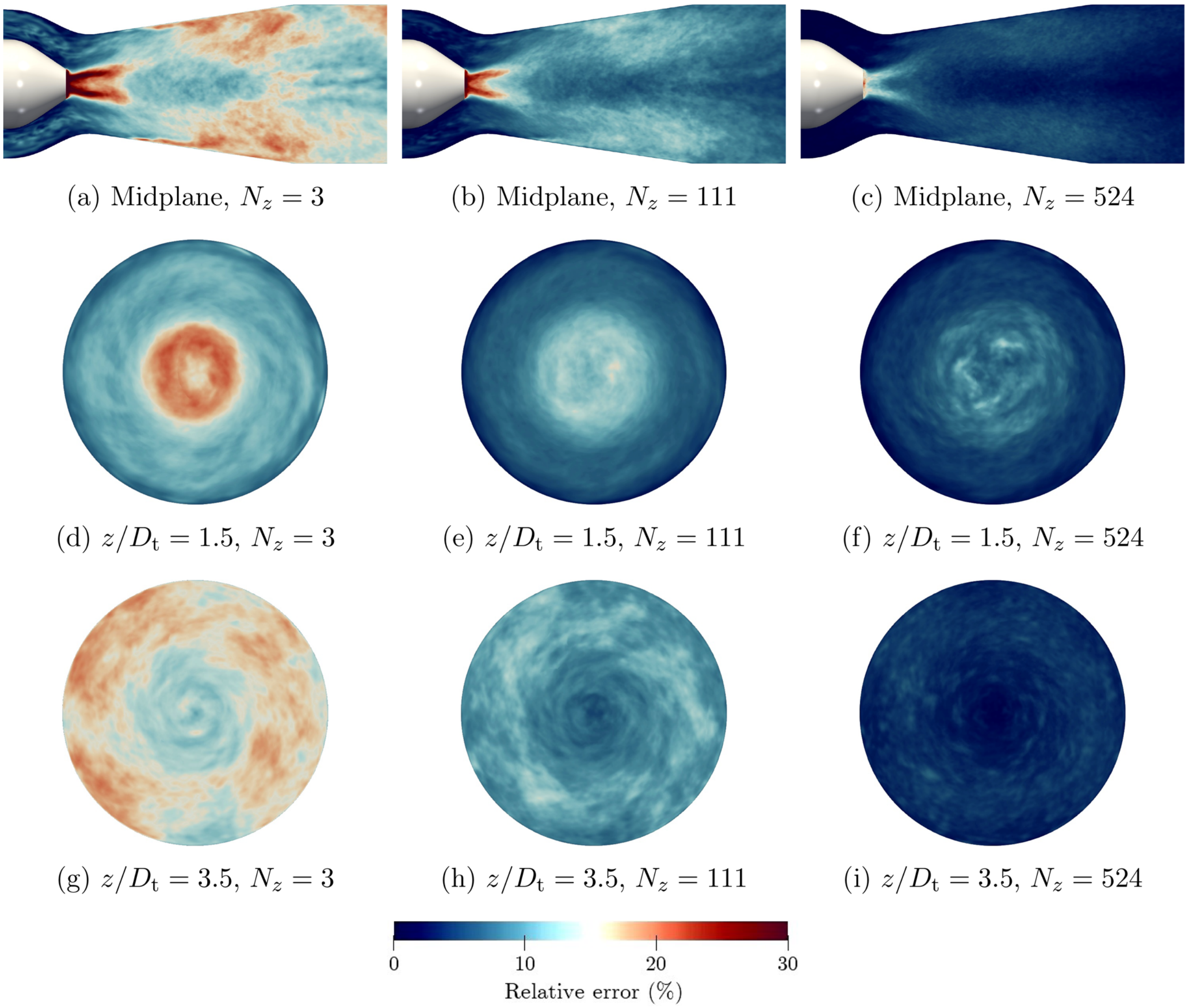
(a) Midplane, $N_z = 3$ (b) Midplane, $N_z = 111$ (c) Midplane, $N_z = 524$

(d) $z/D_\mathrm{t} = 1.5$, $N_z = 3$ (e) $z/D_\mathrm{t} = 1.5$, $N_z = 111$ (f) $z/D_\mathrm{t} = 1.5$, $N_z = 524$

(g) $z/D_\mathrm{t} = 3.5$, $N_z = 3$ (h) $z/D_\mathrm{t} = 3.5$, $N_z = 111$ (i) $z/D_\mathrm{t} = 3.5$, $N_z = 524$

FIG. 27. Time-averaged relative error of the SPDMD reconstruction of the velocity magnitude field using different levels of sparsity.

machine was initially designed to emulate the draft tube instability observed in Francis turbines operating at part load conditions. The CFD computations were performed using the open-source software OpenFOAM. The turbulent flow field was resolved through a fine IDDES simulation. The LES region was shown to be sufficiently resolved (more than 80%) throughout the main region of interest, i.e., the test section. The CFD simulation was verified by an extensive grid study and validated through the comparison of the computed velocity field with the experimental data.

The signal processing of the pressure and force data reveals the existence of a robust vortex rope that precesses with $f/f_\mathrm{n} = 1.19$ (rotating mode) and oscillates axially with $f/f_\mathrm{n} = 0.29$ (plunging mode).

The visualized flow structures through the λ_2 criterion and vorticity contours indicate that the vortex rope is helically wrapped around the stagnant region. The evolving boundary layer on the test section wall separates shortly after the test section throat which leads to instability and disintegration of the vortex rope downstream. A reunited vortex core is formed downstream after the disintegration.

The modal analysis is performed on multiple 2D planes and a 3D coarse mesh onto which the CFD data are interpolated. The slow convergence rate of the cumulative energy of the data matrix POD modes can be attributed to the chaotic and wide-ranging characteristics of turbulent flows, where all scales collectively contribute to the overall flow energy. The distribution of complex eigenvalues exhibits mostly stable modes which is consistent with the stationary nature of the flow. The SPDMD algorithm demonstrated its ability to effectively retrieve the most influential modes by taking into account their overall time contribution.

The FFT analysis of the eigenmodes' time dynamics indicates that the DMD modes indeed include isolated frequencies linked to specific physical phenomena, whereas POD modes display significant spectral leakage across a broad spectrum of frequencies.

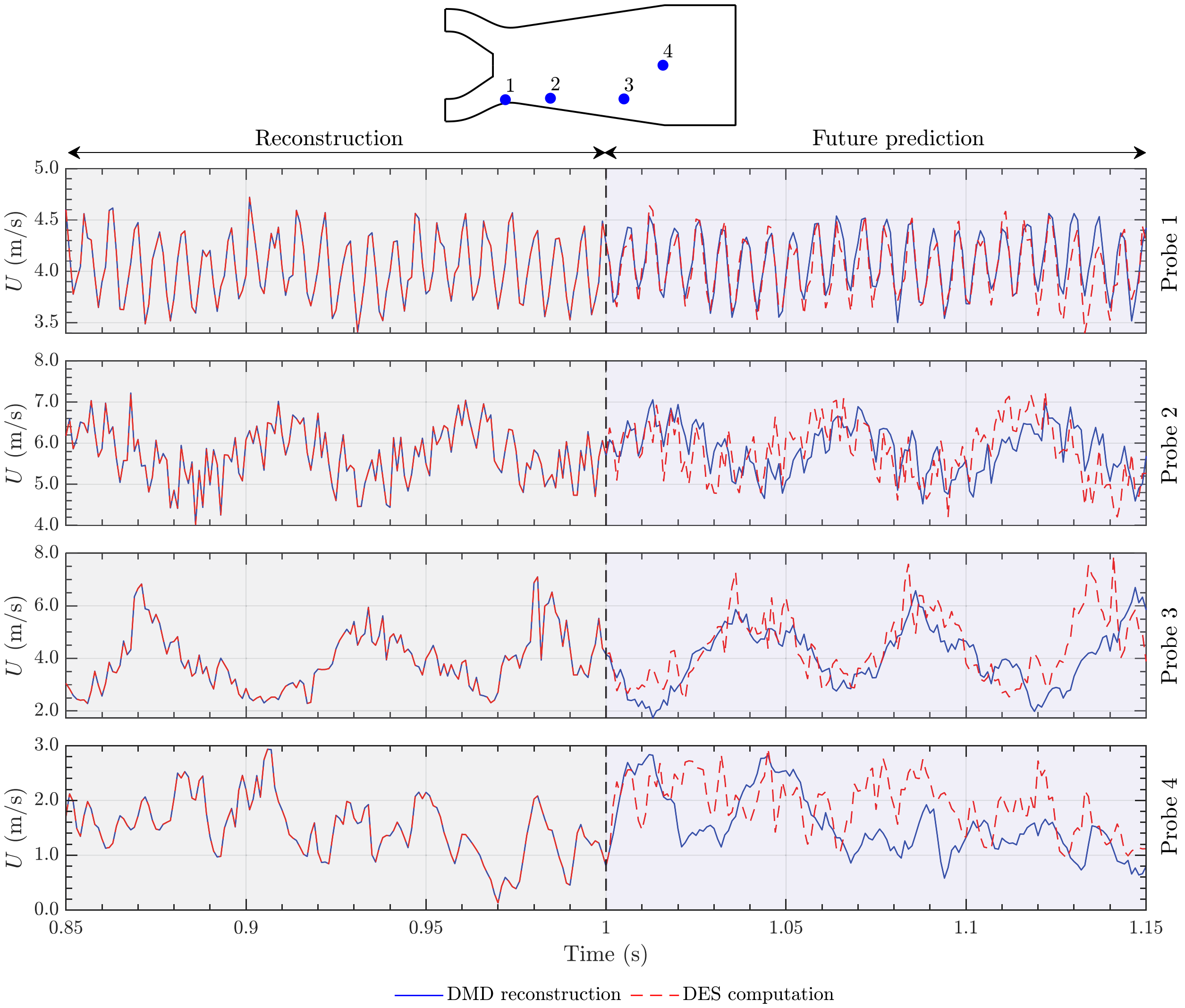

FIG. 28. Reconstruction and prediction of future of velocity magnitude at four probes located on the test section midplane.

The reconstruction of the DMD eigenmodes and their dynamics revealed that the rotating mode, characterized by anti-correlated patterns, is the most dominant mode oscillating with $f/f_\mathrm{n} = 1.21$ in both the midplane and the $z/D_\mathrm{t} = 1.5$ plane. However, downstream at $z/D_\mathrm{t} = 3.5$, where the primary structure disintegrates, the mode representing the downstream reunited vortex corresponding to $f/f_\mathrm{n} = 0.55$ emerges as the most dominant.

Distinct eigenmodes at about $f/f_\mathrm{n} = 0.65$ were identified that represent the boundary layer separation on the test section wall caused by the pronounced adverse pressure gradient. The eigenfrequency associated with the boundary layer separation and reunited vortex phenomena elucidated the origin of the observed peaks at similar frequencies in the FFT analysis of pressure and forces. This finding was made possible through the combined modal and flow analysis, which would not have been achievable through a flow field analysis alone.

Eigenmodes related to the plunging effect and the wakes of the blades were consistently identified at both the midplane and the $z/D_\mathrm{t} = 1.5$ plane. Plunging effect modes exhibited primarily axial oscillations immediately behind the runner crown. However, both plunging and blade wake modes diminish as they move downstream from the test section and become indistinguishable.

Data sequence reconstruction reveals that the essential characteristics of the flow field, such as the rotational dynamics of the vortex rope, can be simplified using just a few DMD modes. Nonetheless, when it comes to reconstructing intricate and localized structures, a larger number of modes is necessary. The most considerable reconstruction error tends to arise in regions with chaotic local eddies, like separated flow areas.

While it is possible to achieve a perfect flow field reconstruction through a full DMD computation, the model typically fails to predict future behavior with an acceptable level of accuracy. The chaotic nature of the resolved turbulent flow field presents a substantial challenge for predicting the future through a model trained on prior events.

The current modal analysis can help in understanding the underlying physics and can ultimately lead to designing effective controlling mechanisms.

ACKNOWLEDGMENTS

The research presented was carried out as a part of the "Swedish Centre for Sustainable Hydropower—SVC." SVC has been established by the Swedish Energy Agency, Energiforsk and Svenska kraftnät together with Luleå University of Technology, Uppsala University, KTH Royal Institute of Technology, Chalmers University of Technology, Karlstad University, Umeå University and Lund University, `svc.energiforsk.se`.

The computations were enabled by resources provided by the National Academic Infrastructure for Supercomputing in Sweden (NAISS) at NSC and C3SE partially funded by the Swedish Research Council through Grant Agreement No. 2022-06725.

AUTHOR DECLARATIONS

Conflict of Interest

The authors have no conflicts to disclose.

Author Contributions

Saeed Salehi: Conceptualization (lead); Data curation (lead); Formal analysis (lead); Funding acquisition (equal); Investigation (lead); Methodology (lead); Project administration (equal); Resources (equal); Software (lead); Validation (lead); Visualization (lead); Writing – original draft (lead); Writing – review & editing (equal). **Håkan Nilsson:** Funding acquisition (equal); Project administration (equal); Resources (equal); Supervision (lead); Writing – review & editing (equal).

DATA AVAILABILITY

The data that support the findings of this study are available from the corresponding author upon reasonable request.

REFERENCES

[1] P. Sorknaes, A. N. Andersen, J. Tang, and S. Strøm, "Market integration of wind power in electricity system balancing," Energy Strategy Rev. **1**, 174–180 (2013).

[2] G. Caralis, D. Papantonis, and A. Zervos, "The role of pumped storage systems towards the large scale wind integration in the Greek power supply system," Renewable Sustainable Energy Rev. **16**, 2558–2565 (2012).

[3] J. Hell, "High flexible hydropower generation concepts for future grids," J. Phys.: Conf. Ser. **813**, 012007 (2017).

[4] M. Nishi, T. Kubota, S. Matsunaga, and Y. Senoo, "Study on swirl flow and surge in an elbow type draft tube," in *Proceedings of the 10th IAHR Symposium*, Tokyo, Japan (1980), Vol. 1, pp. 557–568.

[5] F. Flemming, J. Foust, J. Koutnik, and R. K. Fisher, "Overload surge investigation using CFD data," Int. J. Fluid Mach. Syst. **2**, 315–323 (2009).

[6] W. Rheingans, "Power swings in hydroelectric power plants," Trans. Am. Soc. Mech. Eng. **62**, 171–177 (1940).

[7] A. Glattfelder, H. Grein, and P. Doerfler, "System vibrations in hydro plants," Escher Wyss News **54–55**, 27–31 (1981).

[8] H. Grein, "Vibration phenomena in Francis turbines: Their causes and prevention," Escher Wyss News **54–55**, 37–42 (1981).

[9] M. Nishi, X. Wang, M. Okamoto, and S. Matsunaga, "Further investigation on the pressure fluctuations caused by cavitation vortex rope in an elbow draft tube," in *ASME Symposium on Cavitation and Gas Fluid Flow Machinery and Devices*, FED-Vol. 190 (ASME, New York, 1994), pp. 63–70.

[10] C. Nicolet, A. Zobeiri, P. Maruzewski, and F. Avellan, "Experimental investigations on upper part load vortex rope pressure fluctuations in Francis turbine draft tube," Int. J. Fluid Mach. Syst. **4**, 179–190 (2011).

[11] P. Dörfler, M. Sick, and A. Coutu, *Flow-Induced Pulsation and Vibration in Hydroelectric Machinery: Engineer's Guidebook for Planning, Design and Troubleshooting* (Springer-Verlag, London, 2013).

[12] X. Liu, Y. Luo, and Z. Wang, "A review on fatigue damage mechanism in hydro turbines," Renewable Sustainable Energy Rev. **54**, 1–14 (2016).

[13] A. I. Bosioc, R. Susan-Resiga, S. Muntean, and C. Tanasa, "Unsteady pressure analysis of a swirling flow with vortex rope and axial water injection in a discharge cone," J. Fluids Eng. **134**, 081104 (2012).

[14] J. K. Harvey, "Some observations of the vortex breakdown phenomenon," J. Fluid Mech. **14**, 585–592 (1962).

[15] J. J. Cassidy and H. T. Falvey, "Observations of unsteady flow arising after vortex breakdown," J. Fluid Mech. **41**, 727–736 (1970).

[16] T. Sarpkaya, "On stationary and travelling vortex breakdowns," J. Fluid Mech. **45**, 545–559 (1971).

[17] M. G. Hall, "Vortex breakdown," Annu. Rev. Fluid Mech. **4**, 195–218 (1972).

[18] O. Lucca-Negro and T. O'Doherty, "Vortex breakdown: A review," Prog. Energy Combust. Sci. **27**, 431–481 (2001).

[19] R. Susan-Resiga, S. Muntean, F. Avellan, and I. Anton, "Mathematical modelling of swirling flow in hydraulic turbines for the full operating range," Appl. Math. Modell. **35**, 4759–4773 (2011).

[20] W. Gyllenram, H. Nilsson, and L. Davidson, "On the failure of the quasicylindrical approximation and the connection to vortex breakdown in turbulent swirling flow," Phys. Fluids **19**, 045108 (2007).

[21] M. Fanelli, "The vortex rope in the draft tube of Francis turbines operating at partial load: A proposal for a mathematical model," J. Hydraul. Res. **27**, 769–807 (1989).

[22] R. Susan-Resiga, G. Dan Ciocan, I. Anton, and F. Avellan, "Analysis of the swirling flow downstream a Francis turbine runner," J. Fluids Eng. **128**, 177–189 (2005).

[23] P. A. Kuibin, V. L. Okulov, R. F. Susan-Resiga, and S. Muntean, "Validation of mathematical models for predicting the swirling flow and the vortex rope in a Francis turbine operated at partial discharge," IOP Conf. Ser.: Earth Environ. Sci. **12**, 012051 (2010).

[24] R.-K. Zhang, F. Mao, J.-Z. Wu, S.-Y. Chen, Y.-L. Wu, and S.-H. Liu, "Characteristics and control of the draft-tube flow in part-load Francis turbine," J. Fluids Eng. **131**, 021101 (2009).

[25] H. Foroutan and S. Yavuzkurt, "Flow in the simplified draft tube of a Francis turbine operating at partial load. I. Simulation of the vortex rope," J. Appl. Mech. **81**, 061010 (2014).

[26] S. Salehi, H. Nilsson, E. Lillberg, and N. Edh, "An in-depth numerical analysis of transient flow field in a Francis turbine during shutdown," Renewable Energy **179**, 2322–2347 (2021).

[27] S. Salehi and H. Nilsson, "Flow-induced pulsations in Francis turbines during startup—A consequence of an intermittent energy system," Renewable Energy **188**, 1166–1183 (2022).

[28] S. Salehi and H. Nilsson, "Effects of uncertainties in positioning of PIV plane on validation of CFD results of a high-head Francis turbine model," Renewable Energy **193**, 57 (2022).

[29] S. Salehi and H. Nilsson, "A semi-implicit slip algorithm for mesh deformation in complex geometries, implemented in OpenFOAM," Comput. Phys. Commun. **287**, 108703 (2023).

[30] M. Nishi, "Flow regimes in an elbow-type draft tube," in *Proceedings of the 11th IAHR Symposium on Hydraulic Machinery and System*, Amsterdam (1982), pp. 1–13.

[31] M. Nishi, "Surging characteristics of conical and elbow type draft tubes," in *Proceedings of the 12th IAHR Symposium on Hydraulic Machinery and System*, Stirling (1984), pp. 272–283.

[32] J. Arpe and F. Avellan, "Pressure wall measurements in the whole draft tube: Steady and unsteady analysis," in *Proceedings of the 21st IAHR Symposium on Hydraulic Machinery and Systems*, Lausanne, Switzerland (International Association for Hydraulic Research, 2002), Vol. 1, pp. 593–602.

[33] G. D. Ciocan, M. S. Iliescu, T. C. Vu, B. Nennemann, and F. Avellan, "Experimental study and numerical simulation of the FLINDT draft tube rotating vortex," J. Fluids Eng. **129**, 146–158 (2006).

[34] A. Favrel, A. Müller, C. Landry, K. Yamamoto, and F. Avellan, "Study of the vortex-induced pressure excitation source in a Francis turbine draft tube by particle image velocimetry," Exp. Fluids **56**, 1–15 (2015).

[35] R. Goyal, M. J. Cervantes, and B. K. Gandhi, "Vortex rope formation in a high head model Francis turbine," J. Fluids Eng. **139**, 041102 (2017).

[36] S. Pasche, F. Avellan, and F. Gallaire, "Part load vortex rope as a global unstable mode," J. Fluids Eng. **139**, 051102 (2017).

[37] J. L. Lumley, "The structure of inhomogeneous turbulent flows," *Atmospheric Turbulence and Radio Wave Propagation* (Nauka, 1967), pp. 166–178.

[38] L. Sirovich, "Turbulence and the dynamics of coherent structures. I. Coherent structures," Q. Appl. Math. **45**, 561–571 (1987).

[39] G. Berkooz, P. Holmes, and J. L. Lumley, "The proper orthogonal decomposition in the analysis of turbulent flows," Annu. Rev. Fluid Mech. **25**, 539–575 (1993).

[40] P. Holmes, J. L. Lumley, and G. Berkooz, *Turbulence, Coherent Structures, Dynamical Systems and Symmetry*, Cambridge Monographs on Mechanics (Cambridge University Press, 1996).

[41] D. Stefan and P. Rudolf, "Proper orthogonal decomposition of pressure fields in a draft tube cone of the Francis (Tokke) turbine model," J. Phys.: Conf. Ser. **579**, 012002 (2015).

[42] D. Štefan, P. Rudolf, S. Muntean, and R. Susan-Resiga, "Proper orthogonal decomposition of self-induced instabilities in decelerated swirling flows and their mitigation through axial water injection," J. Fluids Eng. **139**, 081101 (2017).

[43] S. Kumar, S. Khullar, M. J. Cervantes, and B. K. Gandhi, "Proper orthogonal decomposition of turbulent swirling flow of a draft tube at part load," IOP Conf. Ser.: Earth Environ. Sci. **774**, 012091 (2021).

[44] I. Litvinov, D. Sharaborin, E. Gorelikov, V. Dulin, S. Shtork, S. Alekseenko, and K. Oberleithner, "Modal decomposition of the precessing vortex core in a hydro turbine model," Appl. Sci. **12**, 5127 (2022).

[45] C. W. Rowley, I. Mezić, S. Bagheri, P. Schlatter, and D. S. Henningson, "Spectral analysis of nonlinear flows," J. Fluid Mech. **641**, 115–127 (2009).

[46] P. J. Schmid, "Dynamic mode decomposition of numerical and experimental data," J. Fluid Mech. **656**, 5–28 (2010).

[47] B. O. Koopman, "Hamiltonian systems and transformation in Hilbert space," Proc. Natl. Acad. Sci. U.S.A. **17**, 315–318 (1931).

[48] M. R. Jovanović, P. J. Schmid, and J. W. Nichols, "Sparsity-promoting dynamic mode decomposition," Phys. Fluids **26**, 024103 (2014).

[49] Y. Han and L. Tan, "Dynamic mode decomposition and reconstruction of tip leakage vortex in a mixed flow pump as turbine at pump mode," Renewable Energy **155**, 725–734 (2020).

[50] C. Sun, T. Tian, X. Zhu, O. Hua, and Z. Du, "Investigation of the near wake of a horizontal-axis wind turbine model by dynamic mode decomposition," Energy **227**, 120418 (2021).

[51] B. Jiang, G. Sun, Y. Wang, X. Mao, and L. Tan, "Coherent structures decomposition of the flow field in Francis turbine runner under different working conditions," Renewable Energy **186**, 717–729 (2022).

[52] T. W. Muld, G. Efraimsson, and D. S. Henningson, "Flow structures around a high-speed train extracted using proper orthogonal decomposition and dynamic mode decomposition," Comput. Fluids **57**, 87–97 (2012).

[53] M. Kiewat, "Streaming modal decomposition approaches for vehicle aerodynamics," Ph.D. thesis (Technische Universität München, 2019).

[54] M. Zhao, Y. Zhao, and Z. Liu, "Dynamic mode decomposition analysis of flow characteristics of an airfoil with leading edge protuberances," Aerosp. Sci. Technol. **98**, 105684 (2020).

[55] M. Elmore, E. Fernandez, and J. Kapat, "Analysis of heat transfer on turbulence-generating ribs using dynamic mode decomposition," Int. J. Heat Mass Transfer **147**, 118961 (2020).

[56] Z. Huang, T. Li, K. Huang, H. Ke, M. Lin, and Q. Wang, "Predictions of flow and temperature fields in a T-junction based on dynamic mode decomposition and deep learning," Energy **261**, 125228 (2022).

[57] F. Magionesi, G. Dubbioso, R. Muscari, and A. Di Mascio, "Modal analysis of the wake past a marine propeller," J. Fluid Mech. **855**, 469–502 (2018).

[58] M. Liu, L. Tan, and S. Cao, "Dynamic mode decomposition of cavitating flow around ALE 15 hydrofoil," Renewable Energy **139**, 214–227 (2019).

[59] L. Wang, X. Liu, N. Wang, and M. Li, "Modal analysis of propeller wakes under different loading conditions," Phys. Fluids **34**, 065136 (2022).

[60] S. Muthukrishnan, *Data Streams: Algorithms and Applications* (Now Publishers, Inc., 2005).

[61] S. Boyd, N. Parikh, E. Chu, B. Peleato, and J. Eckstein, "Distributed optimization and statistical learning via the alternating direction method of multipliers," Found. Trends Mach. Learn. **3**, 1–122 (2011).

[62] J. Kou and W. Zhang, "An improved criterion to select dominant modes from dynamic mode decomposition," Eur. J. Mech. -B/Fluids **62**, 109–129 (2017).

[63] R. Susan-Resiga and S. Muntean, "Decelerated swirling flow control in the discharge cone of Francis turbines," in *Fluid Machinery and Fluid Mechanics*, edited by J. Xu, Y. Wu, Y. Zhang, and J. Zhang (Springer, Berlin, Heidelberg, 2009), pp. 89–96.

[64] A. Javadi, A. Bosioc, H. Nilsson, S. Muntean, and R. Susan-Resiga, "Experimental and numerical investigation of the precessing helical vortex in a conical diffuser, with rotor–stator interaction," J. Fluids Eng. **138**, 081106 (2016).

[65] A. I. Bosioc, S. Muntean, C. Tanasa, R. Susan-Resiga, and L. Vékás, "Unsteady pressure measurements of decelerated swirling flow in a discharge cone at lower runner speeds," IOP Conf. Ser.: Earth Environ. Sci. **22**, 032008 (2014).

[66] H. G. Weller, G. Tabor, H. Jasak, and C. Fureby, "A tensorial approach to computational continuum mechanics using object-oriented techniques," Comput. Phys. **12**, 620 (1998).

[67] OpenCFD, *OpenFOAM—The Open Source CFD Toolbox—User's Guide, Version v2112*, OpenCFD, Ltd., 2021.

[68] O. Petit, A. I. Bosioc, H. Nilsson, S. Muntean, and R. F. Susan-Resiga, "Unsteady simulations of the flow in a swirl generator, using OpenFOAM," Int. J. Fluid Mach. Syst. **4**, 199–208 (2011).

[69] M. L. Shur, P. R. Spalart, M. K. Strelets, and A. K. Travin, "A hybrid RANS-LES approach with delayed-DES and wall-modelled LES capabilities," Int. J. Heat Fluid Flow **29**, 1638–1649 (2008).

[70] P. R. Spalart, "Comments on the feasibility of LES for wings, and on a hybrid RANS/LES approach," in *Proceedings of the First AFOSR International Conference on DNS/LES* (Greyden Press, Ruston, LA, 1997).

[71] P. R. Spalart, S. Deck, M. L. Shur, K. D. Squires, M. K. Strelets, and A. Travin, "A new version of detached-eddy simulation, resistant to ambiguous grid densities," Theor. Comput. Fluid Dyn. **20**, 181–195 (2006).

[72] A. K. Travin, M. L. Shur, P. R. Spalart, and M. K. Strelets, "Improvement of delayed detached-eddy simulation for LES with wall modelling," in *Proceedings (CDROM) of the European Conference on Computational Fluid Dynamics ECCOMAS CFD*, edited by P. Wesseling, E. Oñate, and J. Périaux (Delft University of Technology, Egmond aan Zee, The Netherlands, 2006).

[73] U. Piomelli, S. Radhakrishnan, L. Zhong, and M. Li, "Wall-layer models for large-eddy simulations of high Reynolds number non-equilibrium flows," in *Advances in Turbulence XI*, edited by J. Palma and A. Lopes (Springer, Berlin, Germany, 2007), pp. 47–54.

[74] C. Mockett, B. Greschner, T. Knacke, R. Perrin, J. Yan, and F. Thiele, "Demonstration of improved des methods for generic and industrial applications," in *Advances in Hybrid RANS-LES Modelling*, edited by S.-H. Peng and W. Haase (Springer, Berlin, Heidelberg, 2008), pp. 222–231.

[75] M. Shur, P. Spalart, M. Strelets, and A. Travin, "Detached-eddy simulation of an airfoil at high angle of attack," in *Engineering Turbulence Modelling and Experiments 4*, edited by W. Rodi and D. Laurence (Elsevier Science Ltd., Oxford, 1999), pp. 669–678.

[76] H. Jasak, "Error analysis and estimation for the finite volume method with applications to fluid flows," Ph.D. thesis (Imperial College, London, 1996).

[77] A. Travin, M. Shur, M. Strelets, and P. R. Spalart, "Physical and numerical upgrades in the detached-eddy simulation of complex turbulent flows," in *Advances in LES of Complex Flows*, edited by R. Friedrich and W. Rodi (Springer, Dordrecht, The Netherlands, 2002), pp. 239–254.

[78] P. Spalart, M. Shur, M. Strelets, and A. Travin, "Sensitivity of landing-gear noise predictions by large-eddy simulation to numerics and resolution," AIAA Paper No. 2012-1174, 2012.

[79]S. Patankar and D. Spalding, "A calculation procedure for heat, mass and momentum transfer in three-dimensional parabolic flows," Int. J. Heat Mass Transfer **15**, 1787–1806 (1972).

[80]R. Issa, "Solution of the implicitly discretised fluid flow equations by operator-splitting," J. Comput. Phys. **62**, 40–65 (1986).

[81]J. P. V. Doormaal and G. D. Raithby, "Enhancements of the simple method for predicting incompressible fluid flows," Numer. Heat Transfer **7**, 147–163 (1984).

[82]C. M. Rhie and W. L. Chow, "Numerical study of the turbulent flow past an airfoil with trailing edge separation," AIAA J. **21**, 1525–1532 (1983).

[83]J. H. Ferziger, M. Perić, and R. L. Street, *Computational Methods for Fluid Dynamics* (Springer, 2002), Vol. 3.

[84]H. Jasak, "Dynamic mesh handling in OpenFOAM," AIAA Paper No. 2009-341, 2009, p. 341.

[85]R. Poletto, T. Craft, and A. Revell, "A new divergence free synthetic eddy method for the reproduction of inlet flow conditions for LES," Flow Turbul. Combust. **91**, 519–539 (2013).

[86]P. Farrell and J. Maddison, "Conservative interpolation between volume meshes by local Galerkin projection," Comput. Methods Appl. Mech. Eng. **200**, 89–100 (2011).

[87]H. J. Aguerre, S. Márquez Damián, J. M. Gimenez, and N. M. Nigro, "Conservative handling of arbitrary non-conformal interfaces using an efficient supermesh," J. Comput. Phys. **335**, 21–49 (2017).

[88]F. Pellegrini and J. Roman, "Scotch: A software package for static mapping by dual recursive bipartitioning of process and architecture graphs," in *High-Performance Computing and Networking*, edited by H. Liddell, A. Colbrook, B. Hertzberger, and P. Sloot (Springer, Berlin, Heidelberg, 1996), pp. 493–498.

[89]W. Gropp, W. D. Gropp, E. Lusk, and A. Skjellum, *Using MPI: Portable Parallel Programming with the Message-Passing Interface* (MIT Press, 1999), Vol. 1.

[90]I. B. Celik, U. Ghia, P. J. Roache, C. J. Freitas, H. Coleman, and P. E. Raad, "Procedure for estimation and reporting of uncertainty due to discretization in CFD applications," J. Fluids Eng. **130**, 078001 (2008).

[91]L. F. Richardson and R. T. Glazebrook, "The approximate arithmetical solution by finite differences of physical problems involving differential equations, with an application to the stresses in a masonry dam," Philos. Trans. R. Soc. London, Ser. A **210**, 307–357 (1911).

[92]L. F. Richardson and J. A. Gaunt, "The deferred approach to the limit," Philos. Trans. R. Soc. London, Ser. A **226**, 299–361 (1927).

[93]A. Bosioc, C. Tanasa, S. Muntean, and R. Susan-Resiga, "2d LDV measurements and comparison with axisymmetric flow analysis of swirling flow in a simplified draft tube," in *Proceedings of the 3rd IAHR International Meeting of Workgroup on Cavitation and Dynamic Problems in Hydraulic Machinery and Systems*, Brno, Czech Republic (2009), pp. 551–560.

[94]A. Javadi and H. Nilsson, "Time-accurate numerical simulations of swirling flow with rotor-stator interaction," Flow Turbul. Combust. **95**, 755–774 (2015).

[95]S. B. Pope, *Turbulent Flows* (Cambridge University Press, 2000).

[96]H. Nyquist, "Certain topics in telegraph transmission theory," Trans. Am. Inst. Electr. Eng. **47**, 617–644 (1928).

[97]C. Shannon, "Communication in the presence of noise," Proc. IRE **37**, 10–21 (1949).

[98]T. Jacob and J.-E. Prénat, "Francis turbine surge: Discussion and data base," in *Hydraulic Machinery and Cavitation*, edited by E. Cabrera, V. Espert, and F. Martínez (Springer, Dordrecht, The Netherlands, 1996), pp. 855–864.

[99]J. Jeong and F. Hussain, "On the identification of a vortex," J. Fluid Mech. **285**, 69–94 (1995).

[100]F. Jin, P. Li, R. Tao, R. Xiao, and D. Zhu, "Study of vortex rope for the flow field pulsation law," Ocean Eng. **273**, 114026 (2023).

[101]J. Garicano-Mena, B. Li, E. Ferrer, and E. Valero, "A composite dynamic mode decomposition analysis of turbulent channel flows," Phys. Fluids **31**, 115102 (2019).

[102]S. Le Clainche and J. M. Vega, "Higher order dynamic mode decomposition," SIAM J. Appl. Dyn. Syst. **16**, 882–925 (2017).

[103]A. Towne, O. T. Schmidt, and T. Colonius, "Spectral proper orthogonal decomposition and its relationship to dynamic mode decomposition and resolvent analysis," J. Fluid Mech. **847**, 821–867 (2018).